molecules

MDPI

Review

Nanostructured MoO_3 for Efficient Energy and Environmental Catalysis

Yuhua Zhu [1,†], Yuan Yao [1,†], Zhu Luo [1], Chuanqi Pan [1], Ji Yang [1], Yarong Fang [1], Hongtao Deng [1,*], Changxiang Liu [2,3], Qi Tan [2], Fudong Liu [2,*] and Yanbing Guo [1,*]

1 Key Laboratory of Pesticide & Chemical Biology of Ministry of Education, Institute of Environmental and Applied Chemistry, College of Chemistry, Central China Normal University, Wuhan 430079, China; zhuyuhua@mails.ccnu.edu.cn (Y.Z.); yaoyuan0711@foxmail.com (Y.Y.); luo.z@mail.ccnu.edu.cn (Z.L.); panchuanqi@mails.ccnu.edu.cn (C.P.); yangji@mails.ccnu.edu.cn (J.Y.); fangyarong@mails.ccnu.edu.cn (Y.F.)

2 Department of Civil, Environmental, and Construction Engineering, Catalysis Cluster for Renewable Energy and Chemical Transformations (REACT), NanoScience Technology Center, University of Central Florida, Orlando, FL 32816, USA; chx-liu@knights.ucf.edu (C.L.); qitan@knights.ucf.edu (Q.T.)

3 Key Laboratory of Chemical Utilization of Plant Resources of Nanchang, College of Science, Jiangxi Agricultural University, Nanchang 330045, China

* Correspondence: denght@mail.ccnu.edu.cn (H.D.); fudong.liu@ucf.edu (F.L.); guoyanbing@mail.ccnu.edu.cn (Y.G.); Tel.: +86-18986037269 (H.D.); +1-407-823-6219 (F.L.); +86-17786507005 (Y.G.)

† These authors contributed equally to this work.

Academic Editor: Titel Jurca

Received: 22 November 2019; Accepted: 15 December 2019; Published: 19 December 2019

Abstract: This paper mainly focuses on the application of nanostructured MoO_3 materials in both energy and environmental catalysis fields. MoO_3 has wide tunability in bandgap, a unique semiconducting structure, and multiple valence states. Due to the natural advantage, it can be used as a high-activity metal oxide catalyst, can serve as an excellent support material, and provide opportunities to replace noble metal catalysts, thus having broad application prospects in catalysis. Herein, we comprehensively summarize the crystal structure and properties of nanostructured MoO_3 and highlight the recent significant research advancements in energy and environmental catalysis. Several current challenges and perspective research directions based on nanostructured MoO_3 are also discussed.

Keywords: nanostructured MoO_3; energy conversion; environmental catalysis; photocatalytic degradation; selective thermocatalysis; water splitting; fuel cells; crystalline structure; morphology

1. Introduction

In the 21st century, the impending depletion of fossil fuels and urgent environmental concerns are among the most challenging issues. Exploration of renewable and sustainable energy and the development of new and improved materials are the solutions to keep environmental sustainability [1–4]. Catalysts are increasingly important in the development of innovative clean energy, environmental protection, and energy conversion [5–7]. Accordingly, the search for developing superior nanostructured catalysts is a sustainable alternative. Noble metal catalysts such as Pt, Pd, Rh, and Au exhibit high activity, to tackle the energy and environmental challenges. However, the noble metal catalysts are impacted by their scarcity, high cost, and relatively low stability, which impede their general use in large scale applications. As a result, catalysts with higher activity and lower cost are urgently required for large-scale practical applications [8]. Transitional metal oxides dominate widespread

applications in energy and environmental catalysis on account of their relatively low cost, high activity, and stability [9–12].

Molybdenum oxide (MoO_3), a kind of transition metal oxide with a n-type semiconducting, nontoxic nature and high stability, has attracted a lot of attention. In particular, nanostructured MoO_3 has demonstrated superior properties to bulk MoO_3, which is successfully employed in rechargeable batteries [13], capacitors [14], photocatalysis [15], electrocatalysis [16], gas sensors [17], and other applications [6]. The extended tunnels between the MoO_6 octahedra in MoO_3 are suitable for insert/de-insert mobile ions, such as H^+ and Li^+, and multiple oxidation states can enable rich redox reactions. Moreover, the superiorities of low cost, chemical stability, high theoretical specific capacity (1117 mA·h/g), and the environmentally friendly nature make nanostructured MoO_3 exceptional electrode materials for rechargeable batteries capacitors [13,18]. MoO_3 has been investigated as the photocatalyst in terms of its anisotropic layered structure for absorbing UV, as well as visible light. Introducing a defect band by H^+ intercalation or oxygen vacancies can create defect state and decrease MoO_3 bandgap, which effectively increase the photocatalytic activity [15]. Each oxygen atom bonds to only one molybdenum atom of MoO_6 octahedra, and oxygen vacancy generates Mo dangling bond. MoO_3 favors the adsorption of water molecules in oxygen vacancies, which act as electron acceptors and consequently reduce the energy barrier make it highly reactive for electrocatalysis [2,19]. As a good gasochromic material, MoO_3 has efficient positive-ion accommodation and good charge transfer, and it can be used as an optical-based gas sensor. Moreover, relying on the change in the conductance of the oxide-on-gas adsorption/reaction, MoO_3 has been used for NO, NO_2, CO, H_2, NH_3, and other gases [17]. The unique structure strongly affects the performances. Large efforts have been made to obtain nanostructured MoO_3 with appealing properties by engineering multiple synthetic strategies for the applications in various fields. A variety of methods have been developed, including hydrothermal method [20], vapor deposition method [21], sol-gel method [22], electrochemical deposition [23], exfoliation method [24], and so forth [25]. Furthermore, many strategies have been used to improve the performance of nanostructured MoO_3 by controlling compositions, crystal facets, structural blocks, and defects, as well as tailoring the interfacial and electronic structures through doping and hybridization.

Though many of the literature studies have reported on nanostructured MoO_3, a thorough overview of nanostructured MoO_3 for efficient energy and environmental catalysis is still lacking so far. Hence, in this paper, we present a comprehensive review of the important advances in nanostructured MoO_3 materials. We comprehensively introduce the crystalline structures and mainly focus on summarizing the exploitation of nanostructured MoO_3 in environmental catalysis and energy conversion. We also provide a brief perspective on the current challenges and opportunities for effectively utilizing nanostructured MoO_3 and taking full advantage of MoO_3 in constructing highly efficient materials.

2. Phase Structure and Morphology of Nanostructured MoO_3

2.1. The Phase Structure of MoO_3

MoO_3 involves four different polymorphs (Figure 1), namely the thermodynamically stable orthorhombic phase (α-MoO_3), the metastable monoclinic phase (β-MoO_3), the hexagonal phase (h-MoO_3), and the high-pressure monoclinic (MoO_3-II) [6,20,26,27]. Each polymorph displays very unique physical and chemical properties, including bandgap energies, refractive indices, and mechanical hardness [28].

Among them, α-MoO_3 has been extensively studied because of its outstanding electrochemical and catalytic activities. α-MoO_3 phase is constituted by corner-sharing [MoO_6] octahedra along [001] and [100] directions. Two sublayers are stacked together by sharing the edges of octahedral along the [001] direction, to form a layer with the orthorhombic symmetry (a = 3.963 Å, b = 13.86 Å, c = 3.696 Å). Furthermore, an anisotropic structure with layers along the [010] direction (b axis) with

weak van der Waals forces leads to the formation of α-MoO_3 (see Figure 1a). The layered structure of α-MoO_3 has relatively higher tolerance to nonstoichiometry such as the unusual pentavalent ion Mo^{5+}, which exhibits high affinity for oxygen, and the layer structure allows the small guest ions (such as Li^+, H^+) to be well accommodated, without structural change in principle [20,29,30]. Mai et al. [31] proved that the conductivity and electroactivity of lithiated MoO_3 nanobelt were highly improved compared to that of a non-lithiated MoO_3 nanobelt.

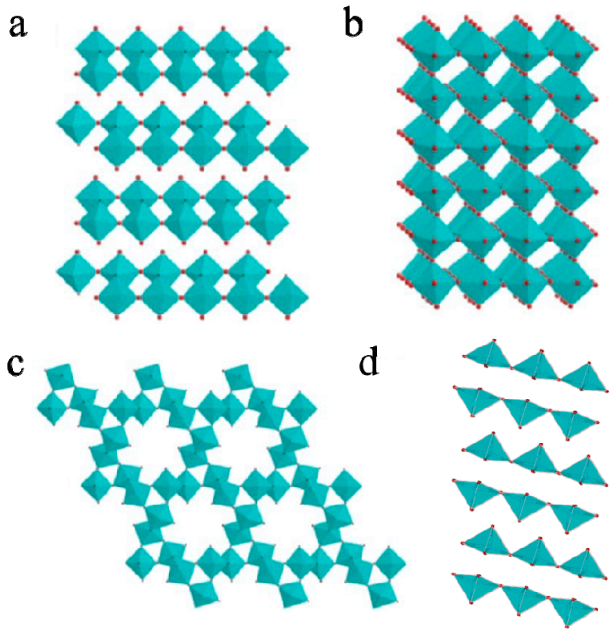

Figure 1. Atomic structures of different crystalline phases of MoO_3. (**a**) α-MoO_3, (**b**) β-MoO_3, (**c**) h-MoO_3, and (**d**) MoO_3-II. Reprinted with permission from [6]. Copyright 2018 American Chemical Society.

The monoclinic structure of β-MoO_3 is markedly different from the crystal structure of α-MoO_3, which possesses a ReO_3-related structure. The MoO_6 octahedral units share corner oxygen atoms in the direction of the c axis, and edge sharing occurs in the direction of the c axis (see Figure 1b). A transformation from the β to α phase took place spontaneously at the temperature ranging from 387 to 450 °C, according to the reported result. Moreover, β-MoO_3 exhibited higher catalytic properties than α-MoO_3 in some catalysis reactions [32–34].

Hexagonal h-MoO_3 is built up by zigzag chains of MoO_6 octahedra linked to each other by corner sharing along the c axis. A very salient crystalline structure for h-MoO_3 is the presence of a tunnel (~ 3.0 Å in diameter) running along the c direction. It can serve as a conduit and intercalation site for mobile ions (see Figure 1c). The h-MoO_3 phase can generally be formulated as $(A_2O)_x{\cdot}MoO_3{\cdot}(H_2O)_y$, where A represents an alkali-metal ion or ammonium ion, and the exact values of x and y depend on the details of the preparation and subsequent treatment [6,26,32,35]. The tunnel structure in h-MoO_3 exhibits considerably higher sensitivity, coloration efficiency, and faster response in comparison with the orthorhombic α-MoO_3. It is mainly attributed to the h-MoO_3 of tunnel structure with a higher structure openness degree, giving rise to an accelerated electron–hole separation in photochromism and a facile Li^+ ion insertion/extraction in electrochromism [36].

High pressure modification of molybdenum trioxide, MoO_3-II (ε-MoO_3), the structure of MoO_3-II is monoclinic, $P2_{l/m}$, with unit cell parameters: a = 3.954(l) Å, b = 3.687(2) Å, c = 7.095(4) Å (see Figure 1d). Like the α-MoO_3 layered structure, the individual $MoO_{3/3}O_{2/2}O_{1/1}$ layers of MoO_3-II and α-MoO_3 are virtually identical. The stacking sequence of the layers of MoO_3-II (aaa) differs from that of α-MoO_3 (aba), which is equated with an improved packing efficiency for the layers of MoO_3-II versus those

of α-MoO_3. The metastable MoO_3-II can convert rapidly to stable orthorhombic phase α-MoO_3 at temperatures above 200 °C, which is relatively more stable than h-MoO_3 [27,28].

The above four different crystal structures have their unique properties, which accordingly influence their applications. The crystal structures of α-MoO_3 and MoO_3-II have distinctive double layers. Some positive ions can easily inject into the layer structure, which can be applied in electrochromism, catalysis, and as an electrode material of lithium ion batteries. However, MoO_3-II is metastable, the crystal structure is easily converted to stable α-MoO_3, which limits its application. The monoclinic structure of β-MoO_3 is a monoclinic ReO_3-related structure, in which each MoO_6 octahedral shares all the corners with adjacent MoO_6 octahedral. Breaking the Mo–O bonds can produce more unsaturated Mo atoms on the surface compared with α-MoO_3, which would behave as active centers for oxidation of small organic molecules, such as partial oxidation of methanol [34]. Unlike α-MoO_3, metastable h-MoO_3 easily permits the ready intercalation and migration of some monovalent cations because of the open structure tunnels. The unique structure would play an important role in enhancing the charge transfer characteristics and displaying an ionic conductive nature. The h-MoO_3 has the potential to exhibit excellent photochromic, electrochromic, and electrochemical properties. Crystal structure is the intrinsic property, but all the stoichiometric MoO_3 phases have wide bandgaps, which seems to impact some applications. Creating oxygen vacancies, reducing crystal dimensions, introducing dopants, or transforming into quantum dots can be used to manipulate the band structure and improve the performance of MoO_3.

2.2. The Morphology of Nanostructured MoO_3

A large number of architectures with controllable sizes or morphologies have been reported to optimize the structure and composition, such as zero-dimensional (0D) quantum dots (QDs), and one-dimensional (1D), two-dimensional (2D), and three-dimensional (3D) architectures, which is significant for revealing the relationship between structure and performance [6].

QDs represent small-size nanocrystals with all three dimensions in several nanometers. The properties were changed significantly from those bulk semiconductors due to their small sizes and the quantum confinement effect [37]. Lu et al. [38] prepared MoO_3 QDs through combining intercalation and thermal exfoliation and studied the optical properties of MoO_3 QDs. The dispersion of MoO_3 QDs showed a tunable strong localized surface plasmon resonance (LSPR) after simulated solar light illumination and the plasmon peak red shifted with an extension of illumination time, which was different from the MoO_3 nanosheets. Lu and co-workers [39] also observed the morphology changes in combination with different photochromic phenomena through preparation of quantum dots from MoO_3 nanosheets by UV irradiation (see Figure 2a). It suggested that the morphology changes were mainly influenced by consumption of photoexcited holes.

One-dimensional structure is mainly used to describe structures of which the growth is along one direction and the one dimension is less than 100 nm. One-dimensional architectures can be divided into nanowires, nanorods, nanotubes, nanobelts, and so on [26,40–45], which are widely used in many fields due to their unique structural traits. For instance, Meduri et al. [40] reported a MoO_{3-x} nanowire array (see Figure 2b). The 1D MoO_3 nanowires could provide good conduction pathways for electronic conductivity, along with a shorter path for lithium diffusion, which showed lower lithium intercalation voltages and flat voltage plateau. One dimensional α-MoO_3 nanorods were prepared with a size of about 50 nm in diameter and few microns long by solution combustion method; the TEM image of α-MoO_3 nanorods is shown in Figure 2c. By comparison and analysis, the thermodynamically stable α-MoO_3 single phase exhibited high specific capacitance and good cycle stability for supercapacitor applications [41]. Single-walled MoO_3 nanotubes were synthesized by Wang and co-workers, and the MoO_3 SWNTs (see Figure 2d) were synthesized by a thiol-assisted hydrothermal method through an interface controlled self-rolling mechanism [42]. Enyashin et al. [43] proposed the atomic models of MoO_3 nanotubes and studied the electronic structure and chemical-bonding indices. The results showed that the holey wall structures of MoO_3 nanotubes made it possible

to dope the materials with various atoms. Moreover, α-MoO_3 nanobelts can display excellent performance for supercapacitors. It was reported that the α-MoO_3 nanobelts' electrode exhibited a higher specific capacitance of 369 F/g and a good cycle stability, with more than 95% of the initial specific capacitance maintained after 500 cycles, which suggested the α-MoO_3 nanobelts could be a potential electrode material [44]. Zheng et al. [26] prepared h-MoO_3 nanobelts and studied the photochromic and electrochromic properties; the TEM image of as-prepared h-MoO_3 nanobelts is shown in Figure 2e. Higher structure openness degree in the tunnel structure of h-MoO_3 could promote electron–hole separation and allow cation insertion/extraction and diffusion which exhibited a better performance on photochromic and electrochromic response than that of α-MoO_3.

Two-dimensional nanostructured MoO_3 attracted extensive attention due to its tunable bandgap and high charge carrier mobility. Balendhran and co-workers presented a 2D MoO_3 based biosensing platform. The nanostructured film made of 2D α-MoO_3 nanoflakes was used as the conduction channel, which significantly reduced response time due to the high permittivity of the 2D α-MoO_3 nanoflakes [46]. In addition, Balendhran et al. [47] also demonstrated that the energy bandgap of 2D high-dielectric α-MoO_3. The α-MoO_3 forming MoO_{3-x} can reduce the bandgap and enhance charge carrier mobility. Compared with the bulk MoO_3, 2D-MoO_3 nanosheets had a better chemical sensor performance due to the 2D structure with a large surface area and more reactive sites [48] (see Figure 2f). Cheng et al. [49] reported that MoO_{3-x} nanosheets can display strong LSPR from the visible to the near-infrared region, owing to the layered crystal structure, which could be used as highly efficient catalysts for the hydrogen generation from ammonia borane with visible light irradiation.

Three-dimensional architectures can increase the surface area and provide more facets with active sites. Three-dimensional architectures mainly include nanoflowers, nanospheres, and mesoporous structures. Nanoflowers can be described as compositions of low-dimensional nano building blocks for certain structures, such as nanorods, nanosheets, and so forth. Sui et al. [50] reported a flower-like α-MoO_3 with hierarchical structure (see Figure 2g). The sensors based on α-MoO_3 flowers exhibited highly sensitive and distinctively selective to trimethylamine. The α-MoO_3 flowers may have less agglomerated configurations, more effective charge transportation, and expose more active sites, as well as specific facets. Another type of promising architecture, nanospheres were widely used in the fields of catalysis, sensing energy storage conversion, and so on [51]. Generally, hollow MoO_3 nanospheres were prepared by drawing support from templates. Triblock copolymer micelles have been used as templates to form hollow MoO_3 nanospheres. The size could be adjusted by choosing a suitable micellar core [52]. Du et al. [53] synthesized highly dispersed MoO_3 nanospheres by ultrasonic irradiation (see Figure 2h) and probed their growth mechanism. Mesoporous structure because of their intrinsic high surface areas and the nano-wall structure were beneficial to diffusing the ions and electrons, which can enhance the electrochemical or photocatalytic properties [6]. Brezesinski and co-workers reported the ordered mesoporous α-MoO_3 nanocrystalline walls for the application of thin-film pseudocapacitors, which exhibited the superior capacitive charge-storage properties compared with both the mesoporous amorphous and nonporous crystalline MoO_3 [54]. Luo et al. also prepared mesoporous MoO_{3-x} (see Figure 2i) with good activity and stability for HER under both acidic and alkaline conditions [55].

Based on the above overview, the performance of MoO_3 is generally influenced by the morphology, and the essence is that the structure of MoO_3 is different. The controllable preparation of diversified nanostructured MoO_3 is an efficient approach to achieve excellent performance. However, it should be noted that some nanostructured MoO_3 with well-controlled morphologies and sizes were not applied well. Hence, it is better to rationally design and synthesize with well-controlled nanostructured MoO_3 based on advances in nanomaterials science and engineering.

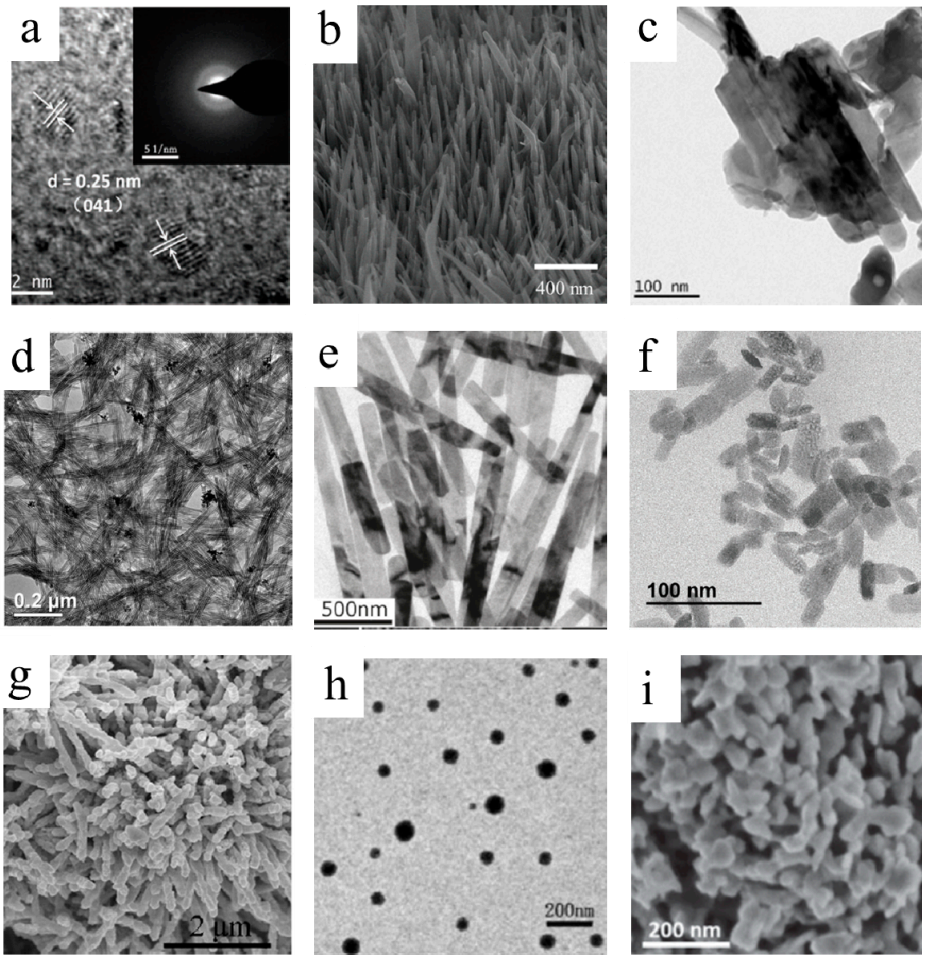

Figure 2. (**a**) HRTEM image of the QDs, the inset shows the SAED pattern of the QDs [39]. Reprinted with permission from [39]. Copyright 2016 The Royal Society of Chemistry. (**b**) SEM image of MoO_{3-x} nanowire array [40]. Reprinted with permission from [40]. Copyright 2012 American Chemical Society. (**c**) TEM image of α-MoO_3 nanorods [41]. Reprinted with permission from [41]. Copyright 2018 Elsevier Ltd. and Techna Group S.r.l. (**d**) Morphology of the obtained single-walled MoO_3 nanotubes [42]. Reprinted with permission from ref 42. Copyright 2008 American Chemical Society. (**e**) TEM image of as-prepared h-MoO_3 nanobelts [26]. Reprinted with permission from [26]. Copyright 2009 American Chemical Society. (**f**) TEM image of MoO_3 nanosheets [48]. Reprinted with permission from [48]. Copyright 2016 The Royal Society of Chemistry. (**g**) SEM image of MoO_3 nanoflowers [50]. Reprinted with permission from [50]. Copyright 2014 Elsevier B.V. (**h**) SEM image of MoO_3 nanospheres [53]. Reprinted with permission from [53]. Copyright 2007 Elsevier B.V. (**i**) SEM image of o mesoporous MoO_{3-x} [55]. Reprinted with permission from [55]. Copyright 2016 WILEY-VCH Verlag GmbH & Co. KGaA, Weinheim.

3. The Application of MoO_3 in Energy Related Catalysis

Due to its low-cost, nontoxicity, multiple oxidation states, and van der Waals gap along the [010] direction, molybdenum oxide (MoO_3) has attracted more and more attention in hydrogen evolution, oxygen evolution, and fuel cells in recent years. However, because of its poor inherent electrical conductivity and slow electrochemical kinetic process, the widespread application of MoO_3 is limited, and a great amount of effort has been devoted to enhancing the catalytic performance of MoO_3.

3.1. Application in Hydrogen Evolution

Owing to high calorific value and its renewable and clean properties, hydrogen (H_2) is regarded as one of the most promising energy carriers for the future. As a layered n-type semiconductor, MoO_3 has been studied as a catalyst for electrocatalytic hydrogen evolution, photocatalytic hydrogen evolution, and ammonia borane dehydrogenation.

3.1.1. Electrocatalytic Hydrogen Evolution Reactions

Electrocatalytic hydrogen evolution reaction (HER) is an efficient method. It is an environmentally friendly process that does not create any by-products. Although the layered structure of MoO_3 is suitable for insertion/removal of small ions such as H^+, MoO_3 always shows poor catalytic performance for HER, due to the lack of active sites [55]. Therefore, MoO_3 always serves as core the substance, as the MoO_3/MoS_2 core–shell structure [56–58]. The MoO_3 core provides high specific surface area and facile charge transport, as depicted in Figure 3a. In order to eliminate the influence of the resistance of the solution and obtain the real kinetic activity of the MoO_3/MoS_2, an iR-corrected test was also performed, and the data is shown in Figure 3b. The HER activity of MoO_3/MoS_2 remained stable even if it was tested for 10,000 cycles (Figure 3c) [56]. Besides, Pt [59], Pd [60], RuO_2 [19] can also load on MoO_3, to get excellent electrocatalysts for electrocatalytic hydrogen evolution.

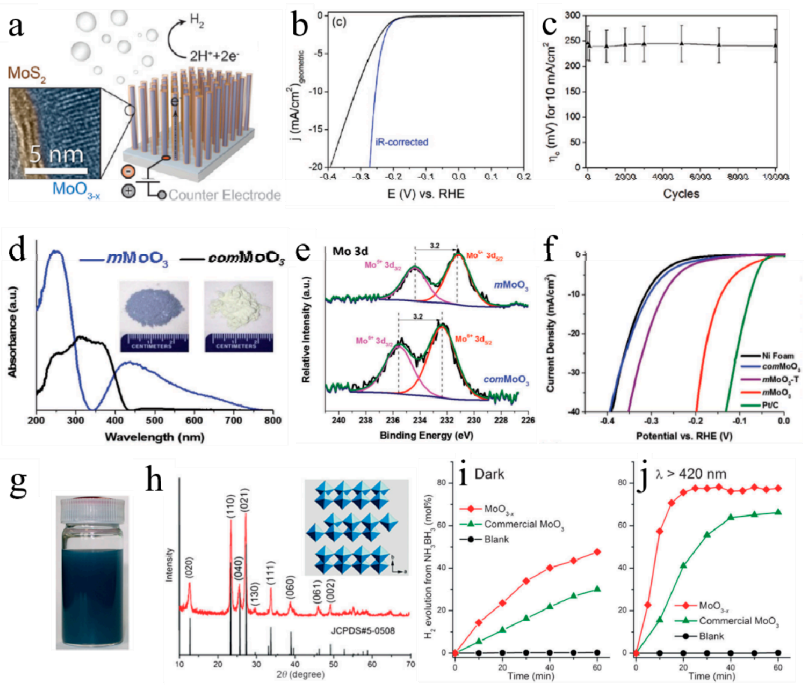

Figure 3. (**a**) Schematic diagram and TEM image of core–shell MoO_3–MoS_2 nanowires applied in hydrogen evolution; (**b**) the HER activity of the nanowires sulfidized at 200 °C is presented with its iR-corrected data; (**c**) the cycling stability of nanowires sulfidized at 200 °C, measured as current density at –0.4 V vs. RHE, normalized to initial current density [56]. Reprinted with permission from [56]. Copyright 2019 American Chemical Society. (**d**) Diffuse reflectance ultraviolet-visible spectra (DR UV-vis) and photos (onset images) for *com*MoO_3 and as-synthesized *m*MoO_3; (**e**) XPS spectrum details for Mo 3d binding energy regions; (**f**) polarization curves of *m*MoO_3 materials on Ni foam electrode in 0.1 M of KOH [55]. Reprinted with permission from [55]. Copyright 2016 WILEY-VCH. (**g**) A photograph of the MoO_{3-x} product dispersed in ethanol; (**h**) XRD pattern of MoO_{3-x} and (inset) crystal structure of the orthorhombic MoO_3. Time course of H_2 evolution from NH_3BH_3 aqueous solution at room temperature for different samples: (**i**) in the dark and (**j**) under visible light irradiation ($\lambda > 420$ nm) [49]. Reprinted with permission from [49]. Copyright 2014 WILEY-VCH.

In order to extend application in electrochemical hydrogen evolution, researchers found that oxygen vacancies can dramatically improve catalytic performance of MoO_3. Figure 3d showed that MoO_3 with oxygen vacancies possessed a much narrower band gap compared to commercial MoO_3, and the color changed from greenish to blue (Figure 3d onset). Figure 3e demonstrates the formation of oxygen vacancies in MoO_3. As shown in Figure 3f, the oxygen vacancies which were close to Mo^{5+} can serve as active sites [55]. In this way, 2D α-MoO_3 nanosheets were fabricated and exhibited a considerable HER performance with low overpotential of 142 mV, to achieve 10 mA/cm^2 current density [61]. Zhang et al. also found that MoO_{3-y} (valence state of V and VI) can be used for efficient electrocatalytic hydrogen evolution [62]. Second, the morphology is another key factor. Mesoporous MoO_3 [55] and MoO_3 nanosheets [61] mentioned above have demonstrated the importance of morphology. Zhang et al. synthesized porous MoO_3 with large specific surface area of 113.8 m^2/g, and it can work as a bifunctional electrocatalyst for (oxygen evolution reactions) OER and HER [63]. The large specific surface area of as-synthesized porous MoO_3 increased electrochemical active area (0.057 mF/cm^2) which was four times bigger than commercial MoO_3 (0.012 mF/cm^2). Third, hetero-atoms doping is another efficient strategy to improve electrocatalytic performance of MoO_3. Li et al. have confirmed that P doped MoO_{3-x} nanosheet (P–MoO_{3-x}) can show the low overpotential of 161 mV to reach 10 mA/cm^2 current density with low Tafel slope of 42 mV per decade [64]. They also found that P doping sites could attract protons to adjacent oxygen vacancies and then form H_{ads} on oxygen vacancies, which meant that P doping sites and oxygen vacancies promoted HER together. Haque et al. also demonstrated that NH_4^+ doped MoO_3 (2D Crys–AMO) just need 138 mV to achieve 10 mA/cm^2 current density. After NH_4^+ doping, orthorhombic MoO_3 was transformed into hexagonal phase, resulting in the formation of highly ordered intracrystalline pores (serve as active sites) [65]. When the hetero-atoms doping leads to the structure defect, such as oxygen vacancies or transformation of intracrystalline phase, the HER activity of MoO_3 may be promoted dramatically. In addition, when the atomic radius of hetero-atoms is similar to oxygen, it may be easier to be doped into the lattice of MoO_3. Stability is another crucial factor for catalysts. In general, MoO_3-based nanocatalysts, which served as substrate or active center, possessed excellent stability in both acid and alkaline media for HER [19,55]. The current density can remain stable at a specific voltage for 12 [55], 24 [19], and even 40 h [65].

3.1.2. Photocatalytic Hydrogen Evolution Reactions

Because solar energy is inexhaustible, photocatalytic hydrogen evolution reaction is an attractive strategy to produce hydrogen from water [66]. MoO_3 is a well-known direct-band-gap semiconductor with high work function and good hole conductivity. However, due to wide band gap energy (about 3.0 eV), the photo-induced electrons/holes (e^-/h^+) pairs are easy to recombine, resulting in low conversion efficiency of incident light [67]. To solve this issue, MoO_3-based nanocomposites were synthesized and studied. Ma et al. fabricated an MoO_3/polyimide composite, and the growth of MoO_3 increased the light absorption and suppressed the recombination of e^-/h^+ pairs [66]. MoO_3–TiO_2 nanotubes were studied, and MoO_3–TiO_2 annealed at 650 °C showed an almost-100-times-higher donor concentration than pure TiO_2 nanotubes. The MoO_3–TiO_2 nanotubes possessed lower charge transfer resistance and improved separation efficiency because of the appearance of MoO_3 [68]. Esparza et al. fabricated a Mo-coated Pt HER catalyst which was O_2-insensitive and stable in acidic media. The formed Mo membrane kept H_2 and O_2 far away from Pt, suppressing both oxygen reduction reactions (ORR) and hydrogen oxidation reactions (HOR). Therefore, the HER efficiency of the Mo-coated Pt HER catalyst was promoted [69]. Guo et al. synthesized MoS_2@MoO_3 core–shell nanowires with a high hydrogen evolution rate of 841.4 μmol/(h·g). The MoO_3 widened the range of light absorption and produced more photo-induced carrier, which accelerated HER rate greatly [70]. Direct bonds formed between CdS NWs and MoO_x clusters were achieved. The MoO_x clusters induced deep electron-trap states by generating long-lived electrons, to improve the activity. The MoO_x clusters could also effectually dissociate adsorbed water molecules, resulting in improved photocatalytic

HER activity [71]. Under light irradiation, no obvious diminution in the photocatalytic activity of MoO_3-based materials for HER was observed for 15–30 h [66–71].

3.1.3. Ammonia Borane Dehydrogenation

Due to nontoxicity, room-temperature stability, and high hydrogen storage content (19.6 wt.%), ammonia borane (NH_3BH_3; AB) has been regarded as an attractive hydrogen storage material candidate [49,72]. With suitable catalysts, the hydrolysis of NH_3BH_3 can be obtained as illustrated in Equation (1):

$$NH_3BH_3 + 2H_2O \rightarrow NH_4^+ + BO_2^- + 3H_2 \quad (1)$$

MoO_3 shows strong LSPR signal, a near-field enhancement phenomenon, in the visible light region. Yamashita group firstly reported visible-light-induced hydrogen evolution enhancement from NH_3BH_3 solution in plasmonic MoO_{3-x} [49], and the blue color of MoO_{3-x} (Figure 3g) was consistent with another report [55]. Figure 3h showed that the MoO_{3-x} is orthorhombic phase. The activity of MoO_{3-x} was obviously higher than commercial MoO_3 under visible light irradiation (Figure 3i,j). After that, they prepared Pd/MoO_{3-x} hybrid and it exhibited great plasmon-enhanced hydrolysis of NH_3BH_3 [72]. The MoO_{3-x} nanoparticles were fabricated, and the enhanced LSPR property generated by the introduction of oxygen vacancies [73]. Further, they explored the effect of reduction temperature to MoO_3, and MoO_{3-x}-200 °C (H_2 reduction temperature) showed a higher dehydrogenation activity [74]. The oxygen vacancies could narrow the band gap of MoO_3, then increased the absorption of visible light in a wider range. Lu et al. synthesized MoO_3-doped $MnCo_2O_4$ microspheres comprised of nanosheets. The Mo doping provided a small pore diameter leading to an enhanced specific surface area (BET area changed from 13.2 to 62.1 m^2/g), which is contributed to enhance hydrolysis of NH_3BH_3 [75]. The stability of existing MoO_3-based catalyst is not desirable due to relatively short test time (60–70 min) [72–75].

In summary, the application of MoO_3 in hydrogen evolution is still in preliminary stage. And the further improvement in the activity and stability is still anticipated. Most of works reported that MoO_3 can serve as substance instead of active center in electrocatalytic and photocatalytic hydrogen evolution. As for NH_3BH_3 dehydrogenation, Yamashita group has been devoted to developing MoO_3 as a promising material. There still exists broad space for the researchers to develop nanostructured MoO_3 as an excellent catalyst for hydrogen evolution. The possible strategy including introduction of oxygen vacancies, hetero-atom doping and hybridization with other materials.

3.2. Application in Oxygen Evolution

3.2.1. Electrocatalytic Oxygen Evolution Reactions

Electrocatalytic OER is another half-reaction of water splitting. Owing to transfer of four electrons for the evolution of an O_2 molecule, OER is more sluggish compared to HER and becomes the rate-determining step of water splitting [76,77]. There are just a few of research studies about MoO_3 applied in OER, in which MoO_3 is regarded to be catalytically inert for OER [78]. Tariq et al. prepared IrO_2–MoO_3 composites and 30% mole fraction of iridium contents, which would be more favorable for OER. The mass specific OER activity of iridium active centers was greatly enhanced by seven-fold [76]. NiO@MoO_3/Vulcan carbon was also investigated by Illathvalappil. The MoO_3 would react with NiO to form a thin $NiMoO_4$ film which could stop MoO_3 from dissolving in the alkaline media, resulting in excellent stability at 1.51 V (vs. RHE) for 15 h in 1 M of KOH solution [77]. Guo et al. fabricated Co-doped MoO_x (CMO) core–shell structure. Figure 4a showed the CMO with uniformly spherical structure of 500 nm in diameter. Further, on a damaged area (Figure 4b), the core–shell structure can be observed, which means that the CMO possesses a MYLIKE chocolate-like structure. And Figure 4c further demonstrated the uniform distribution of Co, Mo, and O in the CMO. The CMO exhibits the overpotential 340 mV to reach 10 mA/cm^2 current density with a Tafel slope of 49 mV per decade (Figure 4d) [78]. The co-doping, bringing numerous active sites (about 6.550×10^{-3} mol/g) and

amorphous structure of the CMO, was responsible for the improvement of OER activity. The durability of these catalysts was not so good, and the current density could remain stable at 10 mA/cm^2 for only 3–15 h in KOH aqueous solution [76–78].

3.2.2. Photoelectrochemical Oxygen Evolution Reactions

Photoelectrochemical (PEC) water splitting has been regarded as a potential avenue for sustainable energy supply. A main obstacle is the need of efficient and stable water oxidation photocatalysts [79,80]. As a high work function (>6.3 eV) and layered semiconductor, MoO_3 always hybridizes with other materials (such as $BiVO_4$) in order to match band potential and obtain an efficient catalyst. Lou et al. fabricated a Bi_2MoO_6/MoO_3 heterojunction by using anodic oxidation of a molybdenum foil and, subsequently, a hydrothermal method at 160 °C for 24 h. The Bi_2MoO_6/MoO_3 photoanode showed about 100% faradic photocurrent-to-O_2 conversion efficiency. They found that, when Bi^{3+} was introduced into the MoO_3 membrane, the valence band moved upward, which would lengthen the wavelength of light absorbed by Bi_2MoO_6/MoO_3. The photocurrent could remain stable for 8 h by using the Bi_2MoO_6/MoO_3 [79]. He et al. prepared the $MoO_3/BiVO_4$ heterojunction film by a drop-casting method, wherein the $BiVO_4$-based precursor was dropped on FTO glass and then dried and annealed. At 0.8 V (vs. SCE), the photocurrent of $MoO_3/BiVO_4$ was six times higher than bare $BiVO_4$ film. The improvement can be attributed to band potentials and conductivity differences between MoO_3 and $BiVO_4$ [80]. $MoO_3/Ag/TiO_2$ nanotube arrays were also successfully synthesized and investigated systemically. The enhanced photoelectrochemical performance is related to the tight contact at the interface. Specifically, the photoinduced electrons could move from valence band of TiO_2 to conduction band of MoO_3 through a Ti–O–Mo bond [81]. Chen et al. prepared Mo-doped $BiVO_4/MoO_x$ electrode (1.2% Mo), and Figure 4e shows the formation of the Mo-doped $BiVO_4/MoO_x$ heterojunction. With the increase of Mo doping amount, MoO_x would gradually accumulate and form a film on the surface of $BiVO_4$, and then continue to grow on the film. At 1.23 V (vs. RHE), the photocurrent density of the catalyst (2.67 mA/cm^2) was five-fold higher than that of $BiVO_4$ electrode [82]. The valence and conduction band edges of $BiVO_4$ and MoO_x are suitable for forming the type II heterojunction at the interface and then accelerate the carrier transfer and separation.

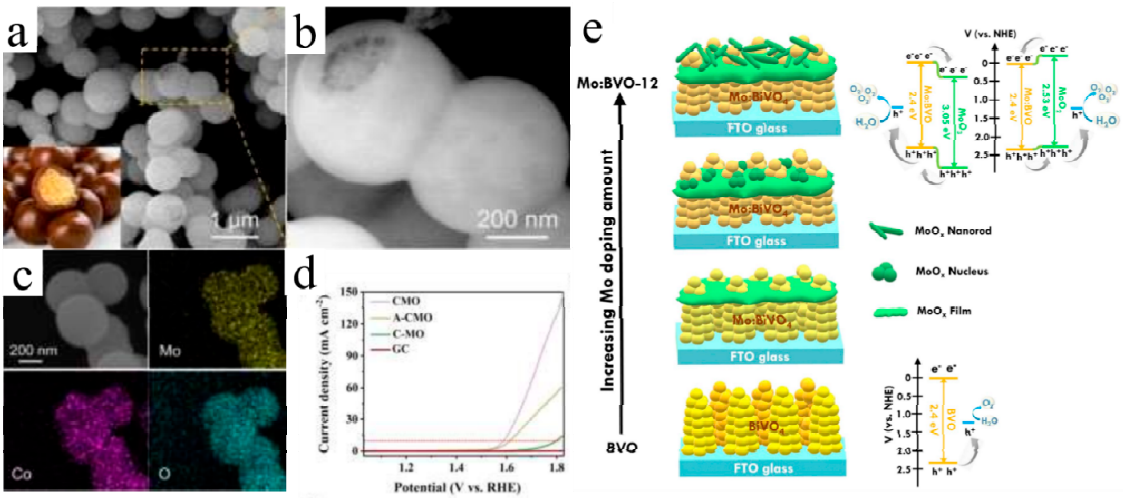

Figure 4. (**a**) SEM image of CoMoOx (inset: the picture of MYLIKES chocolate with unique core–shell structure); (**b**) SEM image of $CoMoO_x$ with high magnitude; (**c**) SEM and element mapping images of Mo, Co, and O in $CoMoO_x$ nanospheres; (**d**) polarization curves comparison between $CoMoO_x$ (CMO), A–$CoMoO_x$, and C–MoO_x [78]. Reprinted with permission from [78]. Copyright 2019 Royal Society of Chemistry. (**e**) The schematic illustration for the formation of the Mo:BVO/MoO_x heterojunction. The band structures along with the charge transfer cascade for the BVO and Mo:BVO-12 electrodes were also shown in the bottom side [82]. Reprinted with permission from [82]. Copyright 2019 Elsevier B.V.

In short summary, the research on MoO_3 for the application of OER and PEC water splitting is limited, but the published reports indicate that MoO_3 is a promising OER and PEC catalyst through morphology and structure design. MoO_3 has a wide band gap (about 3 eV) and easily forms heterojunctions with other materials, so as to obtain photoelectric OER catalysts with higher activity. More effective methods are needed to exploit the potential of MoO_3. Meanwhile, the reason for enhanced catalytic behavior also needs to be further investigated, to provide a principle for designing next-generation electrocatalysts.

3.3. Application in Fuel Cells

3.3.1. Direct Methanol Fuel Cells

With increasing demand of energy, the direct methanol fuel cells (DMFCs) have attracted more and more attention due to their high energy density (5 kW·h/L). However, the low activity of catalysts and the use of noble metals block its commercial application [83–86]. Nonstoichiometric MoO_3 (MoO_x) has a rutile-type structure and shows metallic conductivity, which is relatively stable and highly active [83]. Cabrera et al. first reported Pt/MoO_x/glassy carbon used for DMFCs by using an electrochemical deposition method. The lower valence of molybdenum and the proton spillover effect from hydrogen molybdenum bronze may account for the improved activity [83,84]. Justin et al. also prepared Pt–MoO_3/C composite. Insulating MoO_3 was electrochemically reduced to conductive hydrogen molybdenum bronze ($HxMoO_3$), which can keep the Pt surface clean in order to oxidize methanol. MoO_3 plays a crucial role in the transition process of adsorption intermediates to carbon dioxide [85]. Zhang et al. fabricated Pt/MoO_3 nanowires by using an impregnation–calcination method. After loading of Pt nanoparticles, the Pt/MoO_3 maintained its morphology of nanowires, as shown in Figure 5a. Figure 5b,c shows cyclic voltammetry, linear sweep curves of Pt/MoO_3 and Pt/C, respectively. The Pt/MoO_3 showed much higher electrocatalytic activity and stability for the methanol oxidation, compared to Pt/C (the same Pt loading) [86]. The promoted activity may be attributed to more active catalytic sites and three-dimensional structures generating reactant diffusion microchannels. The stability of MoO_3-based catalysts mentioned above is not satisfactory, and the time of stability test is less than 1 h.

3.3.2. Oxygen-Reduction Reactions

As a type of high efficiency, environmentally friendly energy conversion device, fuel cells have attractive much more attention in recent years [87]. Platinum (Pt) is a benchmark catalyst and always shows excellent performance for ORR. However, it is impossible to use Pt in practical applications that are large in scale because of its scarcity and high cost. Therefore, developing low-content Pt catalysts is a promising way and can be used for real application eventually. Recent researches indicated that MoO_3 can modify a Pt electrode to enhance its catalytic performance and stability [88,89]. After electrodeposition of MoO_3, the Pt/MoO_x/GCE showed a significant increase in the cathodic peak current. The improved performance could be ascribed to the combinations between Pt and MoO_3, which is a doped effect that always happens between transition elements and leads to the optimal mutual electronic density of states [90]. Karuppasamy et al. fabricated Au–MoO_3 and efficiently decreased the usage amount of Au. The Au/MoO_3 exhibited a one-dimensional morphology of nanorods, and there was no obvious aggregation of Au nanoparticles (Figure 5d). Further, according to particle size of statistics, the mean diameter of Au nanoparticles was 5.9 nm (Figure 5e). After 1000 cycles, no obvious change in the half-wave potential was observed, indicating excellent durability. The HRTEM was employed to study the specific structure of Au/MoO_3. The MoO_3 made the appearance of low-coordinated stepped Au atoms in the edge, such as (210), (310), and (410), indicating these were main planes of Au nanoparticles (Figure 5f). Then, Figure 5g,h confirmed that the majority of planes of Au nanoparticles was (111) plane. Due to the presence of MoO_3, the formation of poisonous

intermediates, such as OH species, was suppressed on the high index plane of Au nanoparticles; therefore, oxygen was reduced more efficiently [91].

In summary, the glassy carbon electrodes with Pt-modified MoO_3 have been investigated widely for DMFCs and ORR. The MoO_3 can modify the electronic structure of Pt and suppress the formation of poisonous intermediates on high index plane of Au. However, MoO_3 directly used for DMFCs or ORR has not been reported. This phenomenon may be assigned to the relatively fewer research studies and the fact that MoO_3 always serves as a catalyst of partial oxide, suggesting it does not exist at the active sites for breaking O–O bonds. Besides these points, the oxidation mechanism of methanol and oxygen is complex, and there is no clear mechanism explanation about MoO_3-based materials for DMFCs and ORR. A lot of work still needs to be done for MoO_3-based materials applied in DMFCs and ORR.

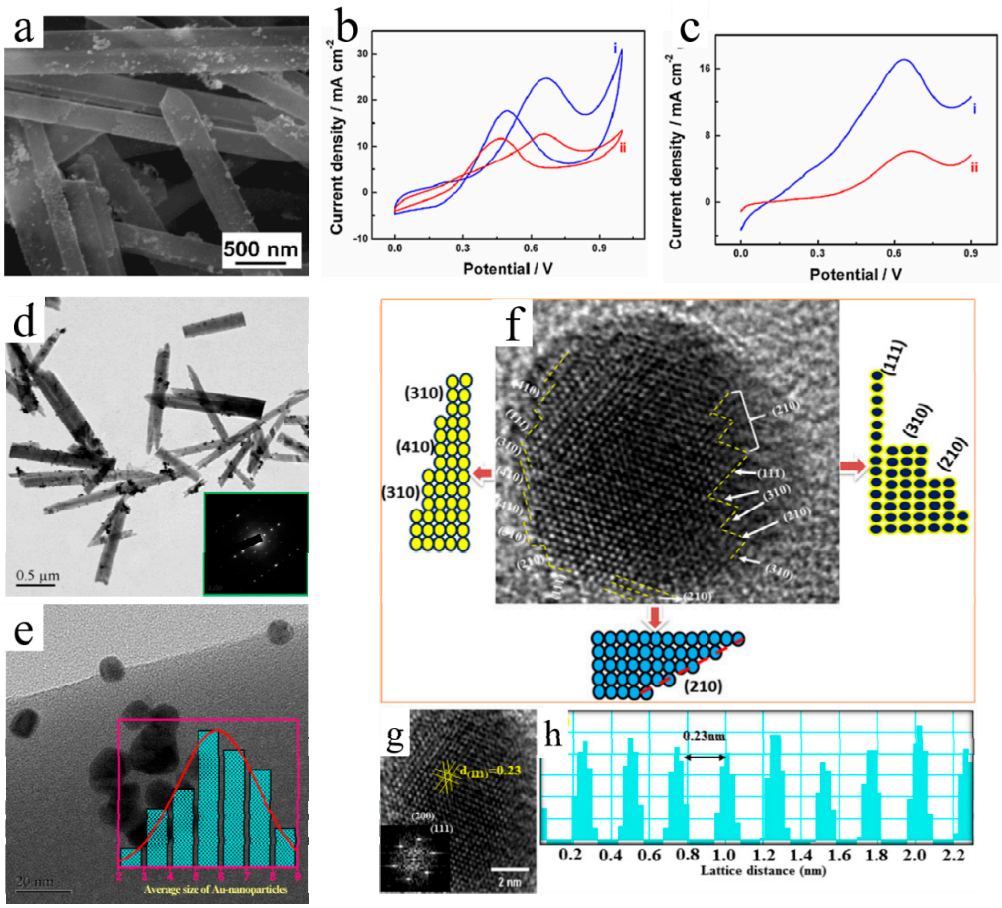

Figure 5. (**a**) FESEM image of the prepared Pt/MoO_3 nanocatalysts; (**b**) CVs of the (i) Pt/MoO_3 and Pt/C (ii) catalysts in 0.5 M of H_2SO_4 containing 1.0 M of CH_3OH; (**c**) LSVs of the (i) Pt/MoO_3 and Pt/C (ii) catalysts in 0.5 M of H_2SO_4 containing 1.0 M of CH_3OH [86]. Reprinted with permission from [86]. Copyright 2015 Elsevier B.V. (**d**) TEM image of Au/MoO_3 (inset: corresponding SAED pattern); (**e**) HRTEM image of Au/MoO_3 (inset: the average size of Au nanocrystals calculated from histograms); (**f**) Typical HRTEM lattice image of high index surfaces Au nanocrystals; (**g**) HRTEM image shows the majority of lattice plane (111) facet of Au nanocrystals, the inset in (**g**) indicates FFT pattern of Au nanocrystals enclosed with (111) and (200) plane; (**h**) IFFT profile of Au nanocrystals lattice distance analysis [91]. Reprinted with permission from [91]. Copyright 2017 Elsevier Ltd.

4. MoO_3 Applied in Environmental Catalysis

4.1. Photodegradation of Organic Pollutants

Photocatalysis is the acceleration of a photoreaction rate in the presence of a catalyst, and it is a green and sustainable catalytic technology that has been widely studied for chemical synthesis, water treatment, environmental cleaning, and self-cleansing processes [92]. The photocatalytic reaction occurs at the interface, based on the absorption of photons with energy larger than the band gap of photocatalyst, with electrons excited from the valence band to the conduction band and producing electron–hole pairs. Photocatalytic efficiency mainly depends on the power and wavelength of the photon source; the properties of the catalyst include its electronic structure, defect density, surface area, and surface-to-volume ratio [93]. Therefore, improving the adsorption capacity of organic pollutants and enhancing the ability of light capture and photo-induced generation performance of electron–hole pairs are important. MoO_3 is one of the most important photocatalysts because of its interesting semiconducting layered structure, rich chemistry associated with multiple valence states and high thermal and chemical stability. Due to the abovementioned outstanding properties, nanostructured MoO_3 has been extensively explored for photocatalytic processes, which are summarized below.

Organic dyes are widely used in textile manufacturing, but they are an environmental threat; hence, the treatment of dyes in wastewater is highly necessary [94]. In general, the degradation rates of rhodamine B (RhB), methylene orange (MO), and methylene blue (MB) are used to evaluate the photocatalytic activity of catalysts. Owing to the distinctive layered structure, MoO_3 exhibited strong adsorption performance and good photocatalytic activity for photodegradation organic pollutants [95–98]. Inadequately, the large band gap (2.7–3.2 eV) of MoO_3 usually limits the photocatalytic performance of decomposing organic pollutants [99,100]. Based on MoO_3, various strategies are employed to develop the new efficient photocatalytic materials with the desired properties. These include the doping collaborated with other applicable semiconductors or elements and the fabrication of composites of heterostructures [15].

Hybrid nanomaterials can be designed to help enhance the degradation efficiency. Lots of efforts have been made in the design of MoO_3-based hybrids such as Eu(Gd)-doped MoO_3 [101,102], rGO/C-MoO_3 [15], and MoO_2/MoO_3 [100]. For instance, Phuruangrat et al. synthesized Gd-doped MoO_3. The Gd-doped MoO_3 nanobelts showed better degradation activity of MB than pure MoO_3, 99% of MB could be degraded by 3 mol% Gd-doped MoO_3 under visible-light irradiation in 60 min (see Figure 6a). MoO_2/MoO_3 hybrid nanostructures were prepared by Xi and co-workers [100]. The photocatalytic activities in RhB degradation for pure MoO_3 and MoO_2/MoO_3 nanocomposites with different contents of MoO_2 under visible-light irradiation are shown in Figure 6b. MoO_2/MoO_3 exhibited high-efficiency degradation for RhB with the assistance of H_2O_2. The ·OH was a dominant reactive species for the degradation of RhB under visible-light irradiation, and the synergistic effect between dyes and MoO_2/MoO_3 nanoparticles accelerated the production of hydroxyl radical (·OH) from H_2O_2 in this system.

Nanocomposites of heterostructures have also been explored to harvest visible-light nanocomposite, and exhibited extremely enhanced visible-light photocatalytic activity for decomposing organic pollutants. Lu et al. [103] fabricated p-MoO_3 nanostructures/n-TiO_2 nanofiber heterojunctions. The p-n nanoheterojunctions decreased photoluminescence intensity, suppressed the recombinations of photogenerated electrons and holes, and enhanced charge separation and photocatalytic efficiencies. Figure 6c–e showed the energy band alignment of p-MoO_3 nanostructures and n-TiO_2 nanofiber heterojunctions and the postulate mechanism for photodegradation of RhB under UV irradiation. Nanostructures/n-TiO_2 nanofiber heterojunctions exhibited a two-times-higher first-order rate constant for the degradation of RhB than that of TiO_2 nanofibers. Significant improvement of the visible-light-driven photodegradation has also been observed, using $Bi_2Mo_3O_{12}$/MoO_3 [104], MoS_2/MoO_3 [105,106], and TiO_2/MoO_3 heterostructures [107]. It was attributed to combining a feasible semiconducting material with MoO_3 to form heterostructural photocatalysts that can enhance the

interfacial charge transfer and minimize the recombination of photogenerated electron–hole pairs, so that the photocatalytic efficiency is greatly improved.

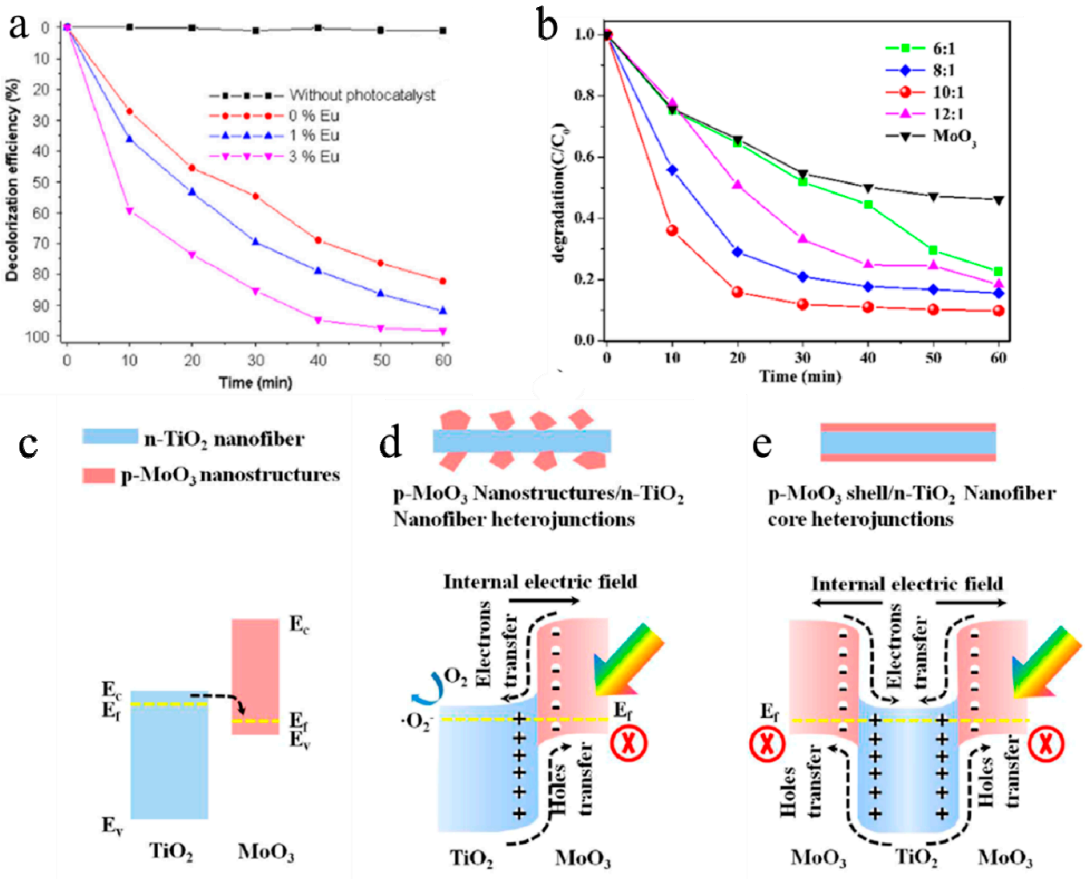

Figure 6. (**a**) Decolorization efficiency of 3 mol% Eu-doped MoO_3 [101]. Reprinted with permission from ref 101. Copyright 2016 Elsevier. (**b**) Photocatalytic activities in RhB degradation for pure MoO_3 and MoO_2/MoO_3 nanocomposites with different contents of MoO_2 under visible-light irradiation [100]. Reprinted with permission from [100]. Copyright 2019 Elsevier. (**c**–**e**) The energy band alignment of p-MoO_3 nanostructures and n-TiO_2 nanofiber heterojunctions and the postulate mechanism for photodegradation of RhB under UV irradiation [103]. Reprinted with permission from [103]. Copyright 2014 American Chemical Society.

Besides, to further shorten degradation period and improve degradation efficiency, the MoO_3-based direct solid-state Z-scheme system with a visible-light-driven semiconductor photocatalysts have been studied. He et al. [108] developed Z-scheme type MoO_3–g-C_3N_4 for enhanced photodegradation activity of methylene orange under visible light irradiation. The high photocatalytic activity of MoO_3–g-C_3N_4 is mainly attributed to the synergetic effect of MoO_3 and g-C_3N_4 in electron–hole pair separation via the charge migration between the two semiconductors (see Figure 7a). Figure 7b showed the PL spectra of MoO_3, g-C_3N_4 and 1.5 wt.% MoO_3–g-C_3N_4 samples. The 1.5 wt.% MoO_3–g-C_3N_4 sample had the strongest PL peak, the reason was the combination of high concentrations of the electron on the CB of g-C_3N_4 and holes on the VB of MoO_3, which generated higher concentration ·OH species. Feng et al. [99] reported AgBr/MoO_3 monolithic catalyst for degrading RhB under visible light irradiation. The formation of well-defined novel Z-scheme between AgBr and MoO_3 effectively accelerated dye-sensitization and charge transfer, resulting in high activity in degrading RhB solution. Figure 7c showed the schematic illustration of photosensitized degradation of the RhB dyes over the AgBr/MoO_3 composite before and after contacting for the AgBr/MoO_3 system. Further experiments suggested that ultrafast degradation of the RhB on the AgBr/MoO_3 nanocomposites was due to both

the photocatalytic process and the dye sensitization. The charge-transfer mechanism was shown in Figure 7d. These results opened up a new avenue in surface- and interface-engineering techniques, enhancing the further utilization in the field of energy transformation and environmental improvement.

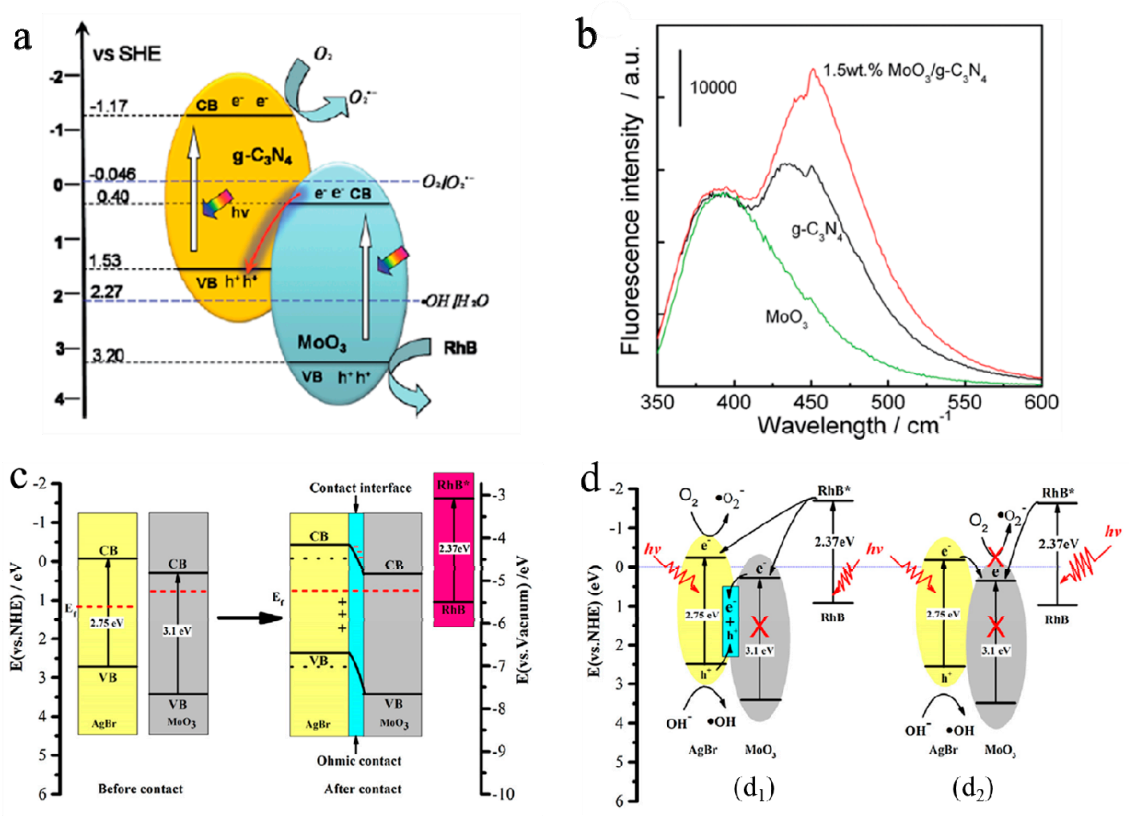

Figure 7. (**a**) Z-scheme mechanism of possible schemes for electron–hole separation and transport at the visible-light-driven MoO_3–g-C_3N_4 composite interface. (**b**) The PL spectra of MoO_3, g-C_3N_4, and 1.5 wt.% MoO_3–g-C_3N_4 samples under visible-light irradiation for 30 min [108]. Reprinted with permission from [108]. Copyright 2014 Royal Society of Chemistry. (**c**) Schematic illustration of photosensitized degradation of the RhB dyes over the AgBr/MoO_3 composite before and after contact. (**d**) Novel Z-scheme (**d_1**), and Heterojunction-type (**d_2**) charge-transfer mechanisms for the AgBr/MoO_3 system [99]. Reprinted with permission from [99]. Copyright 2017 Elsevier B.V.

Apart from the use of decomposing dyes in wastewater, MoO_3 is also effective for photoreduction of aqueous Cr (VI). Very recently, Zhang et al. [109] prepared three-dimensional (3D) MoO_3@ZIF-8 core–shell nanorod composite photocatalysts and studied the Cr (VI) degradation mechanism, which were shown in Figure 8a,b. Compared with the pure ZIF-8 and MoO_3 nanowires, the MoO_3@ZIF-8 catalysts exhibited superior photocatalytic activity for Cr (VI) reduction under visible light (see Figure 8c). The reduction of Cr (VI) was up to 100% with 15% of ZIF-8 in 45 min. Moreover, the composite had good recyclability, and the photocatalytic activity remained almost constant after four cycles. Recently, Jing et al. [110] designed and synthesized Mo_2C/MoO_3 and employed it as catalyst for the photoreduction of Cr (VI) and photodegradation of MO under visible light. The photocatalytic reaction mechanism of photodegradation of MO and photoreduction of Cr (VI) for Mo_2C/MoO_3 under visible-light irradiation was illustrated (see Figure 8d). The Mo_2C/MoO_3 heterostructure showed the good photocatalytic activity for wastewater treatment.

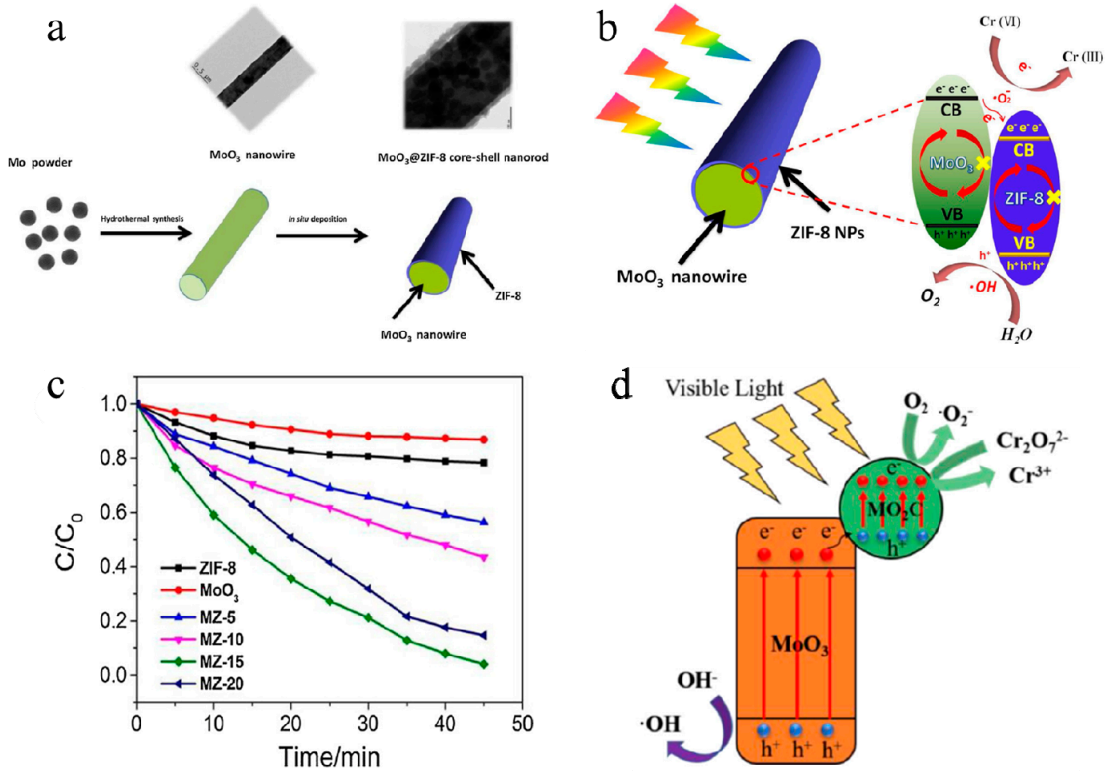

Figure 8. (**a**) Schematic illustration of the synthetic procedure for the hollow MoO_3@ZIF-8 core–shell nanorods. (**b**) Schematic illustration of the Cr (VI) degradation mechanism. (**c**) Photocatalytic performance of MZ-15 under visible-light irradiation [109]. Reprinted with permission from [109]. Copyright 2018 Elsevier B.V. (**d**) The photocatalytic reaction mechanism of photodegradation of MO and photoreduction of Cr (VI) for Mo_2C/MoO_3 under visible-light irradiation [110]. Reprinted with permission from [110]. Copyright 2019 Elsevier.

In brief, MoO_3 has shown a good activity in degradation of the organic pollutants due to the design of morphology, hybrid structure, and heterostructure in catalysts. However, most photocatalytic processes were finished to decompose dyes under visible-light irradiation, so it is meaningful to synthesize nano-photocatalytic materials with a wide variety of wavelength bands. Additionally, based on the reported works, the study of stability and recyclability is poor; however, it is crucial for the practical applications of catalysts.

4.2. Selective Catalysis to Reduce Air Pollutants

4.2.1. Selective Catalytic Reduction of NO_x with NH_3

Nitrogen oxides (NO_x) cause many environmental pollution problems, such as acid rain, photochemical smog, and ozone depletion. Selective catalytic reduction (SCR) of NO_x with NH_3 has become the dominant technology for decreasing NO_x emission from stationary and mobile sources [111,112]. MoO_3 plays an important role in traditional catalysts, for example, with MoO_3-based catalysts for SCR exhibiting good catalytic NO_x removal performance. The redox behavior of V_2O_5–MoO_3/TiO_2 catalysts was investigated by Casagrande and co-workers, who pointed out that the ternary catalysts are more easily reduced and reoxidized than the corresponding binary samples (V_2O_5/TiO_2 and MoO_3/TiO_2 catalysts) [113]. Recently, based on CeO_2/MoO_3 binary or ternary catalysts that were favored by researchers and CeO_2 that possesses excellent redox property also with plenty of Lewis acid sites, the catalysts with MoO_3 loaded on CeO_2 have been well studied, with much more acid sites on surface. The synergistic effect between CeO_2 and MoO_3 contributed to the selective oxidation

of NH_3 to N_2 [114,115]. For instance, Zhu et al. [116] studied the surface structure of $M_xO_y/MoO_3/CeO_2$ system (M = Ni, Cu, Fe) and its influence on SCR of NO by NH_3. The results revealed that the intensity of the interaction between MoO_3 and other metal oxides was different, which could be listed as follows: $NiO/MoO_3/CeO_2$ > $CuO/MoO_3/CeO_2$ > $Fe_2O_3/MoO_3/CeO_2$. The NO conversion for different catalysts in "NO + NH_3 + O_2,' reaction is shown in Figure 9a. Figure 9b shows the schematic drawing of ammonia adsorption and decomposition on Brønsted and Lewis acid sites. The reactivity of "NO + NH_3 + O_2" reaction was strongly associated with acid properties of the catalysts. Additionally, some researchers studied the catalytic behaviors of MoO_3-based catalysts with respect to resistance to phosphorus, as shown in Figure 9c,d. The 1.3P/Ce–Mo(0.5)–O catalyst showed a higher NH_3 reaction rate than the other two catalysts below 350 °C, which suggested that the resistance of the CeO_2 catalyst to phosphate was improved with the addition of Mo, and phosphorus poisoning significantly affected catalyst activity [115]. Nevertheless, the NO_x conversion is still within a relatively narrow temperature window for MoO_3-based NH_3–SCR catalysts, and it is necessary to develop catalysts with superior catalytic performance at both high and low temperatures, with excellent resistance to coexisting poisoning pollutants such as SO_2 and phosphate.

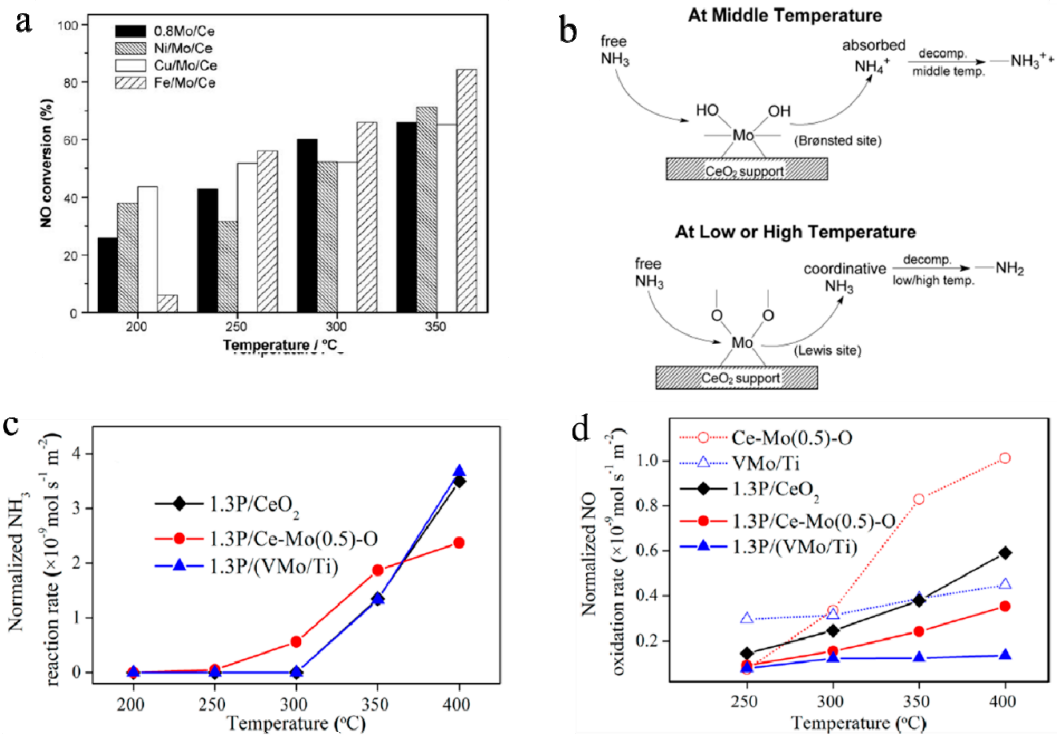

Figure 9. (**a**) The NO conversion for different catalysts in "NO + NH_3 + O_2,' reaction. (**b**) Schematic drawing of ammonia adsorption and decomposition on Brønsted and Lewis acid sites [116]. Reprinted with permission from [116]. Copyright 2009 Elsevier B.V. (**c**) NH_3 reaction rate vs. temperature over the Ce–Mo(0.5)–O and CeO_2 catalysts with different phosphorus content in NH_3 oxidation reaction. (**d**) Normalized NO oxidation rate vs. temperature in NO oxidation reaction over different catalysts after P poisoning [115]. Reprinted with permission from [115]. Copyright 2013 American Chemical Society.

4.2.2. Selective Catalytic Oxidation of Propene

Propene has an extensive production and application in numerous industries, and it is a primary contributor to photochemical smog, making it unfriendly to the environment [117]. There are lots of reports focusing on the catalytic oxidation of propene. MoO_3 is well-known for its structure sensitivity in selective oxidation of propene. The products of selective oxidation mainly include acrylic acid and acrolein. Schuh et al. [118] studied the influence of the morphology of α-MoO_3 in

the selective oxidation of propylene. The results suggested that the morphologies of the samples have a significant effect not only on the selectivity to acrolein, but also on the propylene conversion (see Figure 10a,b). The rod-like structures with (100) facet seemed to be of decisive importance for the catalytic activity, and the same conclusion was drawn by Volta and coworkers [119,120]. Moreover, supported Mo oxides may exhibit different structural and catalytic properties for selective oxidation of propene. Ressler et al. [121] systematically studied the catalytic properties of MoO_3 supported on nanostructured SiO_2 and compared the conversion quantity of h-MoO_3/SiO_2 with that of α-MoO_3 by mass spectrometric analysis of the gas-phase composition during thermal treatment of in propene and oxygen (see Figure 10c). It exhibited stability and catalytic properties different from other binary bulk oxides and could directly oxidize propene to acrylic acid without additional metal sites. Besides this, MoO_3 was used for the epoxidation of propylene to propylene oxide (PO) by molecular oxygen [122]. The work of Jin et al. [123,124] on Ag–MoO_3 and Ag–MoO_3–ZrO_2 catalysts showed that MoO_3 resulted in a significant improvement in the efficiency of the catalyst. The addition of MoO_3 increased the selectivity to 34% at a propylene conversion of 4.6%, whereas the pure Ag catalyst had a PO selectivity of only 0.8% at a propylene conversion of 11%. The olefinic carbon of propylene was easily adsorbed by adding MoO_3 into the silver catalyst. MoO_3 was as an electron and structure-type bifunctional promoter in this system.

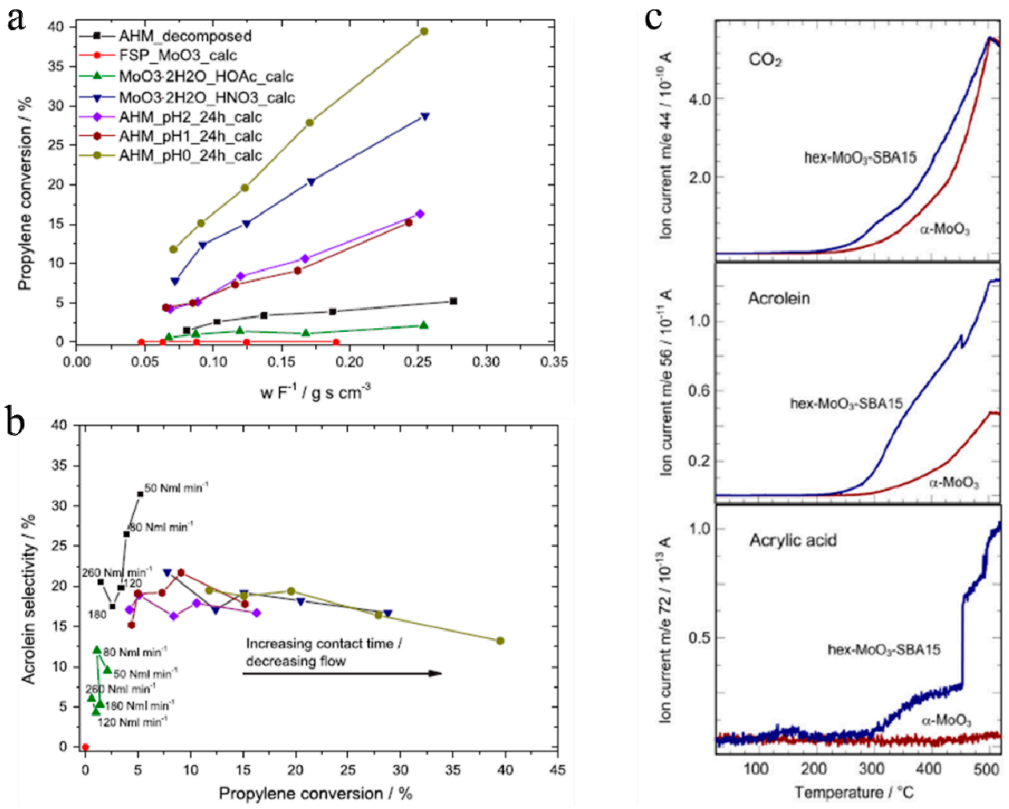

Figure 10. (**a**) The propylene conversion as a function of contact time. (**b**) The acrolein selectivity as a function of propylene conversion [118]. Reprinted with permission from [118]. Copyright 2015 Elsevier B.V. (**c**) Evolution of ion currents of CO_2, acrolein, and acrylic acid obtained by mass spectrometric analysis of the gas phase composition during thermal treatment of MoO_3/SiO_2 or α-MoO_3 in propene and oxygen [121]. Reprinted with permission from [121]. Copyright 2007 Elsevier B.V.

4.2.3. Selective Catalytic Oxidation of Methane

As one of the greenhouse gases, methane effects on global warming. Hence, its emissions have attracted more and more attention [125]. The conversion of CH_4 into chemicals is much more

economical and energy-efficient compared to CO_2. Many publications in this field have been totally committed to the oxidation of methane at relatively high temperature, using transition metal oxides catalysts. The catalysts based on MoO_3 were the most widely studied because of their higher activity and selectivity for methane oxidation [126]. Liu et al. [127] prepared MoO_3/SiO_2 catalysts and studied the kinetics and mechanism of the partial oxidation of methane, using N_2O as the oxidant. These researchers also found that the selective oxidation reaction was initiated by the formation of O^- ions generated from the interaction of N_2O. The structural effects of MoO_3 on partial oxidation of methane to formaldehyde were investigated by Smith et al. The results indicated that Mo=O sites located on the side plane tend to form formaldehyde [128]. Moreover, Arena et al. [129] studied the working mechanism of MoO_3/SiO_2 catalysts in the partial oxidation of methane to Formaldehyde. The influence of the oxide loading on the surface structure and compared with the dispersity of MoO_3/SiO_2 and V_2O_5/SiO_2 catalysts. Taylor et al. [130] prepared a series of catalysts based on MoO_3 and WO_3, the MoO_3 based catalysts were more effective for the production of methanol. The Cu/MoO_3 and Ga_2O_3/MoO_3 catalysts showed selectivity and methanol yield advantage, respectively. MoO_3 demonstrated oxygen insertion ability due to its n-type semiconductivity. However, the mechanism of the co-operative effect in catalysis was not well studied. Most studies focused on the catalytic activity and selectivity, but the research of durability is rather poor.

4.2.4. Other Catalysis to Reduce Air Pollutants

There are only a few reports about MoO_3 catalysts applied for oxidation of CO and some volatile organic compounds (VOCs), such as methanol, $(CH_3)_2S_2$, benzene, and chlorobenzene [131–133]. Mohamed et al. [131] reported the oxidation of CO to CO_2 by MoO_3/CeO_2, and the results suggested that the dispersed MoO_x species and Ce^{3+}/Ce^{4+} redox couples had high capacity toward oxygen, which was most likely to be the active species for CO oxidation. Wang et al. [132] studied the catalytic incineration of $(CH_3)_2S_2$ on $CuO–MoO_3/\gamma\text{-}Al_2O_3$ and the promoter effect. The results revealed that $CuO–MoO_3/\gamma\text{-}Al_2O_3$ has a good activity and durability, and Cr_2O_3 was the most effective promoter. Moreover, MoO_3 as a dopant in $V_2O_5–MoO_3/TiO_2$ catalysts improved redox properties and enhanced chlorobenzene oxidation catalytic activity at a low temperature, and this illuminated new applications for pollutants [133]. These researches will lay an early foundation for exploring MoO_3 catalytic properties in the catalysis of other VOCs.

5. Summary and Outlook

Nanostructured MoO_3 with unique structures and wide availabilities become one of the most promising materials employed for versatile applications. In this review, we have presented the basic structure and main applications of nanostructured MoO_3. The MoO_3 mainly consists of four phases: orthorhombic (α), monoclinic (β), hexagonal (h), and high pressure monoclinic (ε). All of these phases display unique physical and chemical properties for different performances.

We mainly outlined the applications of nanostructured MoO_3 in the field of energy and environmental catalysis, including water splitting, fuel cells, photocatalytic degradation, and selective thermocatalysis. The catalytic activities of nanostructured MoO_3 will be improved through the design of morphology, hybridization, and hybrid structure. The bandgap structure is optimized, and charge transfer is enhanced by constructing heterojunction nanocomposites. Although progress has been made in catalysis based on nanostructured MoO_3, the current research is at nascent stage. It is still required to develop new nanostructured MoO_3 materials to meet more demands in practical applications. For instance, selective catalysis to remove air pollutants requires very high temperatures; therefore, the exploitation of new and improved nanostructured MoO_3 applied to mild conditions is needed. The catalytic nature and mechanism in MoO_3-based catalysts are still challenging and need further studies. Limited research has been done to investigate the stability and recyclability in the selective thermocatalysis. There are numerous research studies about MoO_3 materials used for energy catalysis, especially in the field of hydrogen evolution. All kinds of strategies, including (1) morphology

control, (2) phase transition, (3) introduction of oxygen vacancies, (4) hetero-atom doping, and (5) hybridization with other materials, have been employed to improve catalytic performance and durability of MoO_3-based materials. However, the activity or performance of MoO_3-based materials still do not completely reach the commercial standard, and the mechanism is not fully understood. The strategies mentioned above have been carried out, but there is no systematic and deep study on morphology, phase, oxygen vacancies, etc. Therefore, many problems, such as 'how do oxygen vacancies influence catalytic performance?' still need to be solved. It is more common to see that MoO_3 serves as a support material instead of active centers as a whole. Although some researchers have devoted themselves to addressing this [55,61–65], the activity enhancement is still limited. On the other hand, the durability of MoO_3-based materials still needs to be improved, and the stability test time should be prolonged. Thus, MoO_3 has huge treasure to be excavated for HER, OER, and fuel cells. In short summary, generally speaking, there are two aspects for further studying MoO_3 in the future: (i) the great improvement of catalytic performance and stability; and (ii) insight into structure-activity relationship and mechanism. Novel strategies and new methods must be proposed in order to achieve these long-term goals.

Author Contributions: Literature investigation, analysis, and writing—original draft preparation, Y.Z. and Y.Y.; writing—review and editing, Y.Z., Y.Y., Z.L., C.L., and Q.T.; formal analysis, C.P., J.Y., and Y.F.; design and supervision, H.D., F.L., and Y.G.; project administration, H.D., F.L., and Y.G.; funding acquisition, F.L. and Y.G. All authors have read and agreed to the published version of the manuscript.

Funding: The authors are grateful for the financial support from the National Natural Science Foundation of China (No. 51702112, 21777051, 21707039), the National Engineering Laboratory for Mobile Source Emission Control Technology (NELMS2018A08, NELM-S2017A11), the Open Foundation of State Key Laboratory of Advanced Technology for Materials Synthesis and Processing (Wuhan University of Technology, 2019-KF-8), the Recruitment Program of Global Young Experts start-up funds, the Program of Introducing Talents of Discipline to Universities of China (111 program, B17019), and the Startup Fund from University of Central Florida.

Conflicts of Interest: The authors declare no conflict of interest.

References

1. Ibrahim, I.D.; Sadiku, E.R.; Jamiru, T.; Hamam, Y.; Alayli, Y.; Eze, A.A. Prospects of nanostructured composite materials for energy harvesting and storage. *J. King Saud Univ. Sci.* **2019**, (in press). [CrossRef]
2. Buller, S.; Strunk, J. Nanostructure in energy conversion. *J. Energy Chem.* **2016**, *25*, 171–190. [CrossRef]
3. Li, Y.M.; Somorjai, G.A. Nanoscale advances in catalysis and energy applications. *Nano Lett.* **2010**, *10*, 2289–2295. [CrossRef] [PubMed]
4. Zhang, L.; Zhao, X.S. Carbon-based materials as supercapacitor electrodes. *Chem. Soc. Rev.* **2009**, *38*, 2520–2531. [CrossRef] [PubMed]
5. Zuo, Z.; Wang, D.; Zhang, J.; Lu, F.; Li, Y. Synthesis and applications of graphdiyne-based metal-free catalysts. *Adv. Mater.* **2019**, *31*, 1803762. [CrossRef]
6. Ren, H.; Sun, S.; Cui, J.; Li, X. Synthesis, functional modifications, and diversified applications of molybdenum oxides micro-/nanocrystals: A review. *Cryst. Growth Des.* **2018**, *18*, 6326–6369. [CrossRef]
7. Cui, X.; Tang, C.; Zhang, Q. A review of electrocatalytic reduction of dinitrogen to ammonia under ambient conditions. *Adv. Energy Mater.* **2018**, *8*, 1800369. [CrossRef]
8. Zhang, X.; Lei, J.; Wu, D.; Jing, Y.; Zhou, Z. A Ti-anchored Ti_2CO_2 monolayer (MXene) as a single-atom catalyst for CO oxidation. *J. Mater. Chem. A* **2016**, *4*, 4871–4876. [CrossRef]
9. Sun, S.; Zhang, X.; Yang, Q.; Liang, S.; Zhang, X.; Yang, Z. Cuprous oxide (Cu_2O) crystals with tailored architectures: A comprehensive review on synthesis, fundamental properties, functional modifications and applications. *Prog. Mater. Sci.* **2018**, *96*, 111–173. [CrossRef]
10. Zhao, Y.; Zhang, Y.; Yang, Z.; Yan, Y.; Sun, K. Synthesis of MoS_2 and MoO_2 for their applications in H_2 generation and lithium ion batteries: A review. *Sci. Technol. Adv. Mat.* **2013**, *14*, 043501. [CrossRef]
11. Sun, S.; Liang, S. Morphological zinc stannate: Synthesis, fundamental properties and applications. *J. Mater. Chem. A* **2017**, *5*, 20534–20560. [CrossRef]
12. Sun, S. Recent advances in hybrid Cu_2O-based heterogeneous nanostructures. *Nanoscale.* **2015**, *7*, 10850–10882. [CrossRef] [PubMed]

13. Tang, K.; Farooqi, S.A.; Wang, X.; Yan, C. Recent progress on molybdenum oxides for rechargeable batteries. *ChemSusChem* **2019**, *12*, 755–771. [CrossRef] [PubMed]
14. Van Pham, D.; Patil, R.A.; Yang, C.; Yeh, W.; Liou, Y. Impact of the crystal phase and 3d-valence conversion on the capacitive performance of one-dimensional MoO_2, MoO_3, and Magnéli-phase Mo_4O_{11} nanorod-based pseudocapacitors. *Nano Energy.* **2018**, *47*, 105–114. [CrossRef]
15. Tan, X.; Wang, L.; Cheng, C.; Yan, X.; Shen, B.; Zhang, J. Plasmonic MoO_{3-x}@MoO_3 nanosheets for highly sensitive SERS detection through nanoshell-isolated electromagnetic enhancement. *Chem. Commun.* **2016**, *52*, 2893–2896. [CrossRef] [PubMed]
16. Sinaim, H.; Ham, D.J.; Lee, J.S.; Phuruangrat, A.; Thongtem, S.; Thongtem, T. Free-polymer controlling morphology of α-MoO_3 nanobelts by a facile hydrothermal synthesis, their electrochemistry for hydrogen evolution reactions and optical properties. *J. Alloy. Compd.* **2012**, *512*, 172–178. [CrossRef]
17. Imawan, C.; Steffes, H.; Solzbacher, F.; Obermeier, E. A new preparation method for sputtered MoO_3 multilayers for the application in gas sensors. *Sens. Actuators B* **2001**, *78*, 119–125. [CrossRef]
18. Jiang, F.; Li, W.; Zou, R.; Liu, Q.; Xu, K.; An, L.; Hu, J. MoO_3/PANI coaxial heterostructure nanobelts by in situ polymerization for high performance supercapacitors. *Nano Energy* **2014**, *7*, 72–79. [CrossRef]
19. Sadhanala, H.K.; Harika, V.K.; Penki, T.R.; Aurbach, D.; Gedanken, A. Ultrafine ruthenium oxide nanoparticles supported on molybdenum oxide nanosheets as highly efficient electrocatalyst for hydrogen evolution in acidic medium. *Chemcatchem.* **2019**, *11*, 1495–1502. [CrossRef]
20. Yang, S.; Wang, Z.; Hu, Y.; Luo, X.; Lei, J.; Zhou, D.; Fei, L.; Wang, Y.; Gu, H. Highly responsive room-temperature hydrogen sensing of α-MoO_3 nanoribbon membranes. *ACS Appl. Mater. Interfaces* **2015**, *7*, 9247–9253. [CrossRef]
21. Chen, X.; Lei, W.; Liu, D.; Hao, J.; Cui, Q.; Zou, G. Synthesis and characterization of hexagonal and truncated hexagonal shaped MoO_3 nanoplates. *J. Phys. Chem. C* **2009**, *113*, 21582–21585. [CrossRef]
22. Tang, W.; Liu, L.; Tian, S.; Li, L.; Yue, Y.; Wu, Y.; Zhu, K. Aqueous supercapacitors of high energy density based on MoO_3 nanoplates as anode material. *Chem. Commun.* **2011**, *47*, 10058–10060. [CrossRef] [PubMed]
23. Di Yao, D.; Field, M.R.; O'Mullane, A.P.; Kalantar-zadeh, K.; Ou, J.Z. Electrochromic properties of TiO_2 nanotubes coated with electrodeposited MoO_3. *Nanoscale* **2013**, *5*, 10353–10359. [CrossRef] [PubMed]
24. Alsaif, M.M.Y.A.; Field, M.R.; Daeneke, T.; Chrimes, A.F.; Chrimes, W.; Carey, B.J.; Berean, K.J.; Walia, S.; Embden, J.; Zhang, B.; et al. Exfoliation solvent dependent plasmon resonances in two-dimensional sub-stoichiometric molybdenum oxide nanoflakes. *ACS Appl. Mater. Interfaces* **2016**, *8*, 3482–3493. [CrossRef]
25. Navas, I.; Vinodkumar, R.; Lethy, K.J.; Detty, A.P.; Ganesan, V.; Sathe, V.; Mahadevan Pillai, V.P. Growth and characterization of molybdenum oxide nanorods by RF magnetron sputtering and subsequent annealing. *J. Phys. D Appl. Phys.* **2009**, *42*, 175305. [CrossRef]
26. Zheng, L.; Xu, Y.; Jin, D.; Xie, Y. Novel metastable hexagonal MoO_3 nanobelts: Synthesis, photochromic, and electrochromic properties. *Chem. Mater.* **2009**, *21*, 5681–5690. [CrossRef]
27. McCarron, E.M., III; Calabrese, J.C. The growth and single crystal structure of a high pressure phase of molybdenum trioxide: MoO_3-II. *J. Solid State Chem.* **1991**, *91*, 121–125. [CrossRef]
28. de Castro, I.A.; Datta, R.S.; Ou, J.Z.; Castellanos-Gomez, A.; Sriram, S.; Daeneke, T.; Kalantar-zadeh, K. Molybdenum oxides–from fundamentals to functionality. *Adv. Mater.* **2017**, *29*, 1701619. [CrossRef]
29. Wu, C.; Xie, H.; Li, D.; Liu, D.; Ding, S.; Tao, S.; Chen, H.; Liu, Q.; Chen, S.; Chu, W. Atomically intercalating tin ions into the interlayer of molybdenum oxide nanobelt toward long-cycling lithium battery. *J. Phys. Chem. Lett.* **2018**, *9*, 817–824. [CrossRef]
30. Hu, X.; Zhang, W.; Liu, X.; Mei, Y.; Huang, Y. Nanostructured Mo-based electrode materials for electrochemical energy storage. *Chem. Soc. Rev.* **2015**, *44*, 2376–2404. [CrossRef]
31. Mai, L.Q.; Hu, B.; Chen, W.; Qi, Y.Y.; Lao, C.S.; Yang, R.S.; Dai, Y.; Wang, Z.L. Lithiated MoO_3 nanobelts with greatly improved performance for lithium batteries. *Adv. Mater.* **2007**, *19*, 3712–3716. [CrossRef]
32. Chithambararaj, A.; Rajeswari Yogamalar, N.; Bose, A.C. Hydrothermally synthesized h-MoO_3 and α-MoO_3 nanocrystals: New findings on crystal-structure-dependent charge transport. *Cryst. Growth Des.* **2016**, *16*, 1984–1995. [CrossRef]
33. Mizushima, T.; Fukushima, K.; Ohkita, H.; Kakuta, N. Synthesis of β-MoO_3 through evaporation of HNO_3-added molybdic acid solution and its catalytic performance in partial oxidation of methanol. *Appl. Catal. A* **2007**, *326*, 106–112. [CrossRef]

34. Pham, T.T.P.; Nguyen, P.H.D.; Vo, T.T.; Nguyen, H.H.P.; Luu, C.L. Facile method for synthesis of nanosized β-MoO_3 and their catalytic behavior for selective oxidation of methanol to formaldehyde. *Adv. Nat. Sci. Nanosci. Nanotechnol.* **2015**, *6*, 045010. [CrossRef]
35. Lunk, H.J.; Hartl, H.; Hartl, M.A.; Fait, M.J.; Shenderovich, I.G.; Feist, M.; Frisk, T.A.; Daemen, L.L.; Mauder, D.; Gurinov, A.A. "Hexagonal Molybdenum Trioxide"—known for 100 years and still a fount of new discoveries. *Inorg. Chem.* **2010**, *49*, 9400–9408. [CrossRef]
36. Pan, W.; Tian, R.; Jin, H.; Guo, Y.; Zhang, L.; Wu, X.; Zhang, L.; Han, Z.; Liu, G.; Li, J. Structure, optical, and catalytic properties of novel hexagonal metastable h-MoO_3 nano-and microrods synthesized with modified liquid-phase processes. *Chem. Mater.* **2010**, *22*, 6202–6208. [CrossRef]
37. Xu, S.; Li, D.; Wu, P. One-pot, facile, and versatile synthesis of monolayer MoS_2/WS_2 quantum dots as bioimaging probes and efficient electrocatalysts for hydrogen evolution reaction. *Adv. Funct. Mater.* **2015**, *25*, 1127–1136. [CrossRef]
38. Lu, X.; Wang, R.; Yang, F.; Jiao, W.; Liu, W.; Hao, L.; He, X. Preparation of MoO_3 QDs through combining intercalation and thermal exfoliation. *J. Mater. Chem. C* **2016**, *4*, 6720–6726. [CrossRef]
39. Lu, X.; Wang, R.; Hao, L.; Yang, F.; Jiao, W.; Zhang, J.; Peng, P.; Liu, W. Preparation of quantum dots from MoO_3 nanosheets by UV irradiation and insight into morphology changes. *J. Mater. Chem. C* **2016**, *4*, 11449–11456. [CrossRef]
40. Meduri, P.; Clark, E.; Kim, J.H.; Dayalan, E.; Sumanasekera, G.U.; Sunkara, M.K. MoO_{3-x} nanowire arrays as stable and high-capacity anodes for lithium ion batteries. *Nano Lett.* **2012**, *12*, 1784–1788. [CrossRef]
41. Prakash, N.G.; Dhananjaya, M.; Narayana, A.L.; Shaik, D.P.; Rosaiah, P.; Hussain, O.M. High performance one dimensional α-MoO_3 nanorods for supercapacitor applications. *Ceram. Int.* **2018**, *44*, 9967–9975. [CrossRef]
42. Hu, S.; Wang, X. Single-walled MoO_3 nanotubes. *Am. Chem. J.* **2008**, *130*, 8126–8127. [CrossRef] [PubMed]
43. Enyashin, A.N.; Ivanovskaya, V.V.; Ivanovskii, A.L. Electronic properties and chemical bonding of single-walled MoO_3 nanotubes. *Mendeleev Commun.* **2004**, *14*, 94–95. [CrossRef]
44. Jiang, J.; Liu, J.; Peng, S.; Qian, D.; Luo, D.; Wang, Q.; Tian, Z.; Liu, Y. Facile synthesis of α-MoO_3 nanobelts and their pseudocapacitive behavior in an aqueous Li_2SO_4 solution. *J. Mater. Chem. A* **2013**, *1*, 2588–2594. [CrossRef]
45. Peng, H.; Ma, G.; Mu, J.; Sun, K.; Lei, Z. Low-cost and high energy density asymmetric supercapacitors based on polyaniline nanotubes and MoO_3 nanobelts. *J. Mater. Chem. A* **2014**, *2*, 10384–10388. [CrossRef]
46. Balendhran, S.; Walia, S.; Alsaif, M.; Nguyen, E.P.; Ou, J.Z.; Zhuiykov, S.; Sriram, S.; Bhaskaran, M.; Kalantar-zadeh, K. Field effect biosensing platform based on 2D α-MoO_3. *ACS Nano* **2013**, *7*, 9753–9760. [CrossRef]
47. Balendhran, S.; Deng, J.; Ou, J.Z.; Walia, S.; Scott, J.; Tang, J.; Wang, K.L.; Field, M.R.; Russo, S.; Zhuiykov, S.; et al. Enhanced charge carrier mobility in two-dimensional high dielectric molybdenum oxide. *Adv. Mater.* **2013**, *25*, 109–114. [CrossRef]
48. Ji, F.; Ren, X.; Zheng, X.; Liu, Y.; Pang, L.; Jiang, J.; Liu, S.F. 2D-MoO_3 nanosheets for superior gas sensors. *Nanoscale* **2016**, *8*, 8696–8703. [CrossRef]
49. Cheng, H.; Kamegawa, T.; Mori, K.; Yamashita, H. Surfactant-free nonaqueous synthesis of plasmonic molybdenum oxide nanosheets with enhanced catalytic activity for hydrogen generation from ammonia borane under visible light. *Angew. Chem. Int. Ed.* **2014**, *53*, 2910–2914. [CrossRef]
50. Sui, L.L.; Xu, Y.M.; Zhang, X.F.; Cheng, X.L.; Gao, S.; Zhao, H.; Cai, Z.; Huo, L.H. Construction of three-dimensional flower-like α-MoO_3 with hierarchical structure for highly selective triethylamine sensor. *Sens. Actuators B* **2015**, *208*, 406–414. [CrossRef]
51. Yu, L.; Wu, H.B.; Lou, X.W.D. Self-templated formation of hollow structures for electrochemical energy applications. *Acc. Chem. Res.* **2017**, *50*, 293–301. [CrossRef] [PubMed]
52. Liu, T.; Xie, Y.; Chu, B. Use of block copolymer micelles on formation of hollow MoO_3 nanospheres. *Langmuir* **2000**, *16*, 9015–9022. [CrossRef]
53. Du, K.; Fu, W.; Wei, R.; Yang, H.; Xu, J.; Chang, L.; Yu, Q.; Zou, G. Ultrasonic-assisted synthesis of highly dispersed MoO_3 nanospheres using 3-mercaptopropyltrimethoxysilane. *Ultrason. Sonochem.* **2008**, *15*, 233–238. [CrossRef] [PubMed]
54. Brezesinski, T.; Wang, J.; Tolbert, S.H.; Dunn, B. Ordered mesoporous α-MoO_3 with iso-oriented nanocrystalline walls for thin-film pseudocapacitors. *Nat. Mater.* **2010**, *9*, 146–151. [CrossRef] [PubMed]

55. Luo, Z.; Miao, R.; Huan, T.D.; Mosa, I.M.; Poyraz, A.S.; Zhong, W.; Cloud, J.E.; Kriz, D.A.; Thanneeru, S.; He, J.; et al. Mesoporous MoO_{3-x} material as an efficient electrocatalyst for hydrogen evolution reactions. *Adv. Energy Mater.* **2016**, *6*, 1600528. [CrossRef]
56. Chen, Z.; Cummins, D.; Reinecke, B.N.; Clark, E.; Sunkara, M.K.; Jaramillo, T.F. Core-shell MoO_3-MoS_2 nanowires for hydrogen evolution: A functional design for electrocatalytic materials. *Nano Lett.* **2011**, *11*, 4168–4175. [CrossRef]
57. Jin, B.; Zhou, X.; Huang, L.; Lickleder, M.; Yang, M.; Schmuki, P. Aligned MoO_x/MoS_2 core-shell nanotubular structures with a high density of reactive sites based on self-ordered anodic molybdenum oxide nanotubes. *Angew. Chem. Int. Ed.* **2016**, *55*, 12252–12256. [CrossRef]
58. Cummins, D.R.; Martinez, U.; Sherehiy, A.; Kappera, R.; Martinez-Garcia, A.; Schulze, R.K.; Jasinski, J.; Zhang, J.; Gupta, R.K.; Lou, J.; et al. Efficient hydrogen evolution in transition metal dichalcogenides via a simple one-step hydrazine reaction. *Nat. Commun.* **2016**, *7*, 11857. [CrossRef]
59. Liu, W.; Xu, Q.; Yan, P.; Chen, J.; Du, Y.; Chu, S.; Wang, J. Fabrication of a single-atom platinum catalyst for the hydrogen evolution reaction: A new protocol by utilization of H_xMoO_{3-x} with plasmon resonance. *ChemCatChem* **2018**, *10*, 946–950. [CrossRef]
60. Li, J.; Cheng, Y.; Zhang, J.; Fu, J.; Yan, W.; Xu, Q. Confining Pd nanoparticles and atomically dispersed Pd into defective MoO_3 nanosheet for enhancing electro-and photocatalytic hydrogen evolution performances. *ACS Appl. Mater. Interfaces* **2019**, *11*, 27798–27804. [CrossRef]
61. Datta, R.S.; Haque, F.; Mohiuddin, M.; Carey, B.J.; Syed, N.; Zavabeti, A.; Zhang, B.; Khan, H.; Berean, K.J.; Ou, J.Z. Highly active two dimensional α-MoO_{3-x} for the electrocatalytic hydrogen evolution reaction. *J. Mater. Chem. A* **2017**, *5*, 24223–24231. [CrossRef]
62. Zhang, W.; Li, H.; Firby, C.J.; Al-Hussein, M.; Elezzabi, A.Y. Oxygen vacancy tunable electrochemical properties of electrodeposited molybdenum oxide films. *ACS Appl. Mater. Interfaces* **2019**, *11*, 20378–20385. [CrossRef] [PubMed]
63. Zhang, M.; Li, R.; Hu, D.; Huang, X.; Liu, Y.; Yan, K. Porous molybdenum trioxide as a bifunctional electrocatalyst for oxygen and hydrogen evolution. *J. Electroanal. Chem.* **2019**, *836*, 102–106. [CrossRef]
64. Li, L.; Zhang, T.; Yan, J.; Cai, X.; Liu, S. P Doped MoO_{3-x} Nanosheets as efficient and stable electrocatalysts for hydrogen evolution. *Small* **2017**, *13*, 1700441. [CrossRef]
65. Haque, F.; Zavabeti, A.; Zhang, B.Y.; Datta, R.S.; Yin, Y.; Yi, Z.; Wang, Y.; Mahmood, N.; Pillai, N.; Syed, N.; et al. Ordered intracrystalline pores in planar molybdenum oxide for enhanced alkaline hydrogen evolution. *J. Mater. Chem. A* **2019**, *7*, 257–268. [CrossRef]
66. Ma, C.; Zhou, J.; Cui, Z.; Wang, Y.; Zou, Z. In situ growth MoO_3 nanoflake on conjugated polymer: An advanced photocatalyst for hydrogen evolution from water solution under solar light. *Sol. Energy Mater. Sol. Cells* **2016**, *150*, 102–111. [CrossRef]
67. Pang, X.; Bian, H.; Su, M.; Ren, Y.; Qi, J.; Ma, H.; Wu, D.; Hu, L.; Du, B.; Wei, Q. Photoelectrochemical cytosensing of RAW264.7 macrophage cells based on a TiO_2 nanoneedls@MoO_3 array. *Anal. Chem.* **2017**, *89*, 7950–7957. [CrossRef]
68. Yang, M.; Zhang, L.; Jin, B.; Huang, L.; Gan, Y. Enhanced photoelectrochemical properties and water splitting activity of self-ordered MoO_3-TiO_2 nanotubes. *Appl. Surf. Sci.* **2016**, *364*, 410–415. [CrossRef]
69. Garcia-Esparza, A.T.; Shinagawa, T.; Ould-Chikh, S.; Qureshi, M.; Peng, X.; Wei, N.; Anjum, D.H.; Clo, A.; Weng, T.C.; Nordlund, D.; et al. An oxygen-insensitive hydrogen evolution catalyst coated by a molybdenum-based layer for overall water splitting. *Angew. Chem. Int. Ed.* **2017**, *56*, 5780–5784. [CrossRef]
70. Guo, S.; Li, X.; Ren, X.; Yang, L.; Zhu, J.; Wei, B. Optical and electrical enhancement of hydrogen evolution by MoS_2@MoO_3 core-shell nanowires with designed tunable plasmon resonance. *Adv. Funct. Mater.* **2018**, *28*, 1802567. [CrossRef]
71. Zhang, H.; Zhang, P.; Qiu, M.; Dong, J.; Zhang, Y.; Lou, X.W. Ultrasmall MoO_x clusters as a novel cocatalyst for photocatalytic hydrogen evolution. *Adv. Mater.* **2019**, *31*, 1804883.
72. Cheng, H.; Qian, X.; Kuwahara, Y.; Mori, K.; Yamashita, H. A plasmonic molybdenum oxide hybrid with reversible tunability for visible-light-enhanced catalytic reactions. *Adv. Mater.* **2015**, *27*, 4616–4621. [CrossRef] [PubMed]

73. Shi, J.; Kuwahara, Y.; Wen, M.; Navlani-García, M.; Mori, K.; An, T.; Yamashita, H. Room-temperature and aqueous-phase synthesis of plasmonic molybdenum oxide nanoparticles for visible-light-enhanced hydrogen generation. *Chem. - Asian J.* **2016**, *11*, 2377–2381. [CrossRef] [PubMed]
74. Yin, H.; Kuwahara, Y.; Mori, K.; Cheng, H.; Wen, M.; Yamashita, H. High-surface-area plasmonic MoO_{3-x}: Rational synthesis and enhanced ammonia borane dehydrogenation activity. *J. Mater. Chem. A* **2017**, *5*, 8946–8953. [CrossRef]
75. Lu, D.; Feng, Y.; Ding, Z.; Liao, J.; Zhang, X.; Liu, H.R.; Li, H. MoO_3-doped $MnCo_2O_4$ microspheres consisting of nanosheets: An inexpensive nanostructured catalyst to hydrolyze ammonia borane for hydrogen generation. *Nanomaterials* **2019**, *9*, 21. [CrossRef] [PubMed]
76. Tariq, M.; Zaman, W.Q.; Sun, W.; Zhou, Z.; Wu, Y.; Cao, L.M.; Yang, J. Unraveling the beneficial electrochemistry of IrO_2/MoO_3 hybrid as a highly stable and efficient oxygen evolution reaction catalyst. *ACS Sustain. Chem. Eng.* **2018**, *6*, 4854–4862. [CrossRef]
77. Illathvalappil, R.; George, L.; Kurungot, S. Coexisting few-layer assemblies of NiO and MoO_3 deposited on vulcan carbon as an efficient and durable electrocatalyst for water oxidation. *ACS Appl. Energy Mater.* **2019**, *2*, 4987–4998. [CrossRef]
78. Guo, C.; Sun, X.; Kuang, X.; Gao, L.; Zhao, M.; Qu, L.; Zhang, Y.; Wu, D.; Ren, X.; Wei, Q. Amorphous Co-doped MoO_x nanospheres with a core-shell structure toward an effective oxygen evolution reaction. *J. Mater. Chem. A* **2019**, *7*, 1005–1012. [CrossRef]
79. Lou, S.N.; Scott, J.; Iwase, A.; Amal, R.; Ng, Y.H. Photoelectrochemical water oxidation using a Bi_2MoO_6/MoO_3 heterojunction photoanode synthesised by hydrothermal treatment of an anodised MoO_3 thin film. *J. Mater. Chem. A* **2016**, *4*, 6964–6971. [CrossRef]
80. He, H.; Zhou, Y.; Ke, G.; Zhong, X.; Yang, M.; Bian, L.; Lv, K.; Dong, F. Improved surface charge transfer in $MoO_3/BiVO_4$ heterojunction film for photoelectrochemical water oxidation. *Electrochim. Acta* **2017**, *257*, 181–191. [CrossRef]
81. Yao, Y.; Sun, M.; Zhang, Z.; Lin, X.; Gao, B.; Anandan, S.; Liu, W. In situ synthesis of $MoO_3/Ag/TiO_2$ nanotube arrays for enhancement of visible-light photoelectrochemical performance. *Int. J. Hydrogen Energy* **2019**, *44*, 9348–9358. [CrossRef]
82. Chen, Y.S.; Lin, L.Y. Facile synthesis of Bi-functional molybdenum-doped $BiVO_4$/Molybdenum oxide heterojunction as the photocatalyst for water oxidation. *J. Power Sources* **2019**, *434*, 226705. [CrossRef]
83. Zhang, H.; Wang, Y.; Fachini, E.R.; Cabrera, C.R. Electrochemically codeposited platinum/molybdenum oxide electrode for catalytic oxidation of methanol in acid solution. *Electrochem. Solid-State Lett.* **1999**, *2*, 437–439. [CrossRef]
84. Wang, Y.; Fachini, E.R.; Cruz, G.; Zhu, Y.; Ishikawa, Y.; Colucci, J.A.; Cabrera, C.R. Effect of surface composition of electrochemically codeposited platinum/molybdenum oxide on methanol oxidation. *J. Electrochem. Soc.* **2001**, *148*, 222–226. [CrossRef]
85. Justin, P.; Rao, G.R. Methanol oxidation on MoO_3 promoted Pt/C electrocatalyst. *Int. J. Hydrogen Energy* **2011**, *36*, 5875–5884. [CrossRef]
86. Zhang, H.; Yao, G.; Wang, L.; Su, Y.; Yang, W.; Lin, Y. 3D Pt/MoO_3 nanocatalysts fabricated for effective electrocatalytic oxidation of alcohol. *Appl. Surf. Sci.* **2015**, *356*, 294–300. [CrossRef]
87. Shao, M.; Chang, Q.; Dodelet, J.P.; Chenitz, R. Recent advances in electrocatalysts for oxygen reduction reaction. *Chem. Rev.* **2016**, *116*, 3594–3657. [CrossRef]
88. Cakar, I.; Özdokur, K.V.; Demir, B.; Yavuz, E.; Demirkol, D.O.; Koçak, S.; Timurb, S.; Ertaş, F.N. Molybdenum oxide/platinum modified glassy carbon electrode: A novel electrocatalytic platform for the monitoring of electrochemical reduction of oxygen and its biosensing applications. *Sens. Actuators B* **2013**, *185*, 331–336. [CrossRef]
89. Liu, X.; Wang, H.; Chen, S.; Qi, X.; Gao, H.; Hui, Y.; Bai, Y.; Guo, L.; Ding, W.; Wei, Z. SO_2-tolerant $Pt\text{-}MoO_3/C$ catalyst for oxygen reduction reaction. *J. Energy Chem.* **2014**, *23*, 358–362. [CrossRef]
90. Yavuz, E.; Özdokur, K.V.; Çakar, İ.; Koçak, S.; Ertaş, F.N. Electrochemical preparation, characterization of molybdenum-oxide/platinum binary catalysts and its application to oxygen reduction reaction in weakly acidic medium. *Electrochim. Acta* **2015**, *151*, 72–80. [CrossRef]
91. Karuppasamy, L.; Chen, C.Y.; Anandan, S.; Wu, J.J. High index surfaces of Au-nanocrystals supported on one-dimensional MoO_3-nanorod as a bi-functional electrocatalyst for ethanol oxidation and oxygen reduction. *Electrochim. Acta* **2017**, *246*, 75–88. [CrossRef]

92. Liu, X.; Iocozzia, J.; Wang, Y.; Cui, X.; Chen, Y.; Zhao, S.; Li, Z.; Lin, Z. Noble metal–metal oxide nanohybrids with tailored nanostructures for efficient solar energy conversion, photocatalysis and environmental remediation. *Energy Env. Sci.* **2017**, *10*, 402–434. [CrossRef]
93. Hu, C.; Xu, M.; Zhang, J.; Zhou, Y.; Hu, B.; Yu, G. Recyclable MoO_3 nanobelts for photocatalytic degradation of Rhodamine B by near infrared irradiation. *Int. J. Chem. Kinet.* **2019**, *51*, 3–13. [CrossRef]
94. Etman, A.S.; Abdelhamid, H.N.; Yuan, Y.; Wang, L.; Zou, X.; Sun, J. Facile water-based strategy for synthesizing MoO_{3-x} nanosheets: Efficient visible light photocatalysts for dye degradation. *ACS Omega* **2018**, *3*, 2193–2201. [CrossRef]
95. Gao, B.; Fan, H.; Zhang, X.; Zhu, C. Template-free hydrothermal synthesis of α-molybdenum trioxide nanobelts and their photocatalytic activity for degradation of methylene blue. *Micro Nano Lett.* **2013**, *8*, 500–503. [CrossRef]
96. Ma, Y.; Jia, Y.; Jiao, Z.; Wang, L.; Yang, M.; Bi, Y.; Qi, Y. Facile synthesize α-MoO_3 nanobelts with high adsorption property. *Mater. Lett.* **2015**, *157*, 53–56. [CrossRef]
97. Szkoda, M.; Trzciński, K.; Siuzdak, K.; Lisowska-Oleksiak, A. Photocatalytical properties of maze-like MoO_3 microstructures prepared by anodization of Mo plate. *Electrochim. Acta* **2017**, *228*, 139–145. [CrossRef]
98. Liu, Y.; Feng, P.; Wang, Z.; Jiao, X.; Akhtar, F. Novel fabrication and enhanced photocatalytic MB degradation of hierarchical porous monoliths of MoO_3 nanoplates. *Sci. Rep.* **2017**, *7*, 1845. [CrossRef]
99. Feng, B.; Wu, Z.; Liu, J.; Zhu, K.; Li, Z.; Jin, X.; Hou, Y.; Xi, Q.; Cong, M.; Liu, P.; et al. Combination of ultrafast dye-sensitized-assisted electron transfer process and novel Z-scheme system: AgBr nanoparticles interspersed MoO_3 nanobelts for enhancing photocatalytic performance of RhB. *Appl. Catal. B* **2017**, *206*, 242–251. [CrossRef]
100. Xi, Q.; Liu, J.; Wu, Z.; Bi, H.; Li, Z.; Zhu, K.; Zhuang, J.; Chen, J.; Lu, S.; Huang, Y.; et al. In-situ fabrication of MoO_3 nanobelts decorated with MoO_2 nanoparticles and their enhanced photocatalytic performance. *Appl. Surf. Sci.* **2019**, *480*, 427–437. [CrossRef]
101. Phuruangrat, A.; Cheed-Im, U.; Thongtem, T.; Thongtem, S. High visible light photocatalytic activity of Eu-doped MoO_3 nanobelts synthesized by hydrothermal method. *Mater. Lett.* **2016**, *172*, 166–170. [CrossRef]
102. Phuruangrat, A.; Cheed-Im, U.; Thongtem, T.; Thongtem, S. Influence of Gd dopant on photocatalytic properties of MoO_3 nanobelts. *Mater. Lett.* **2016**, *173*, 158–161. [CrossRef]
103. Lu, M.; Shao, C.; Wang, K.; Lu, N.; Zhang, X.; Zhang, P.; Zhang, M.; Li, X.; Liu, Y. *p*-MoO_3 nanostructures/n-TiO_2 nanofiber heterojunctions: Controlled fabrication and enhanced photocatalytic properties. *ACS Appl. Mater. Interfaces* **2014**, *6*, 9004–9012. [CrossRef] [PubMed]
104. Liu, T.; Li, B.; Hao, Y.; Yao, Z. MoO_3-nanowire membrane and $Bi_2Mo_3O_{12}/MoO_3$ nano-heterostructural photocatalyst for wastewater treatment. *Chem. Eng. J.* **2014**, *244*, 382–390. [CrossRef]
105. Balendhran, S.; Walia, S.; Nili, H.; Ou, J.Z.; Zhuiykov, S.; Kaner, R.B.; Sriram, S.; Bhaskaran, M.; Kalantar-zadeh, K. Two-dimensional molybdenum trioxide and dichalcogenides. *Adv. Funct. Mater.* **2013**, *23*, 3952–3970. [CrossRef]
106. Li, H.; Yu, K.; Tang, Z.; Fu, H.; Zhu, Z. High photocatalytic performance of a type-II α-MoO_3@MoS_2 heterojunction: From theory to experiment. *Phys. Chem. Chem. Phys.* **2016**, *18*, 14074–14085. [CrossRef]
107. Liu, H.; Lv, T.; Zhu, C.; Zhu, Z. Direct bandgap narrowing of TiO_2/MoO_3 heterostructure composites for enhanced solar-driven photocatalytic activity. *Sol. Energy Mater. Sol. Cells* **2016**, *153*, 1–8. [CrossRef]
108. He, Y.; Zhang, L.; Wang, X.; Wu, Y.; Lin, H.; Zhao, L.; Weng, W.; Wan, H.; Fan, M. Enhanced photodegradation activity of methyl orange over Z-scheme type MoO_3–gC_3N_4 composite under visible light irradiation. *RSC Adv.* **2014**, *4*, 13610–13619. [CrossRef]
109. Zhang, Y.; Park, S.J. Facile construction of MoO_3@ ZIF-8 core-shell nanorods for efficient photoreduction of aqueous Cr (VI). *Appl. Catal. B* **2019**, *240*, 92–101. [CrossRef]
110. Jing, X.; Peng, X.; Sun, X.; Zhou, W.; Wang, W.; Wang, S. Design and synthesis of Mo_2C/MoO_3 with enhanced visible-light photocatalytic performance for reduction of Cr (VI) and degradation of organic pollutants. *Mater. Sci. Semicond. Process.* **2019**, *100*, 262–269. [CrossRef]
111. Jiang, Y.; Bao, C.; Liu, Q.; Liang, G.; Lu, M.; Ma, S. A novel CeO_2-MoO_3-WO_3/TiO_2 catalyst for selective catalytic reduction of NO with NH_3. *Catal. Commun.* **2018**, *103*, 96–100. [CrossRef]
112. Geng, Y.; Chen, X.; Yang, S.; Liu, F.; Shan, W. Promotional effects of Ti on a CeO_2–MoO_3 catalyst for the selective catalytic reduction of NOx with NH_3. *ACS Appl. Mater. Interfaces* **2017**, *9*, 16951–16958. [CrossRef]

113. Casagrande, L.; Lietti, L.; Nova, I.; Forzatti, P.; Baiker, A. SCR of NO by NH_3 over TiO_2-supported V_2O_5–MoO_3 catalysts: Reactivity and redox behavior. *Appl. Catal. B* **1999**, *22*, 63–77. [CrossRef]
114. Yu, W.; Zhu, J.; Qi, L.; Sun, C.; Gao, F.; Dong, L.; Chen, Y. Surface structure and catalytic properties of MoO_3/CeO_2 and $CuO/MoO_3/CeO_2$. *J. Colloid Interface Sci.* **2011**, *364*, 435–442. [CrossRef]
115. Chang, H.; Jong, M.T.; Wang, C.; Qu, R.; Du, Y.; Li, J.; Hao, J. Design strategies for P-containing fuels adaptable CeO_2–MoO_3 catalysts for DeNOx: Significance of phosphorus resistance and N_2 selectivity. *Env. Sci. Technol.* **2013**, *47*, 11692–11699. [CrossRef]
116. Zhu, J.; Gao, F.; Dong, L.; Yu, W.; Qi, L.; Wang, Z.; Dong, L.; Chen, Y. Studies on surface structure of $M_xO_y/MoO_3/CeO_2$ system (M = Ni, Cu, Fe) and its influence on SCR of NO by NH_3. *Appl. Catal. B* **2010**, *95*, 144–152. [CrossRef]
117. He, C.; Cheng, J.; Zhang, X.; Douthwaite, M.; Pattisson, S.; Hao, Z. Recent advances in the catalytic oxidation of volatile organic compounds: A review based on pollutant sorts and sources. *Chem. Rev.* **2019**, *119*, 4471–4568. [CrossRef]
118. Schuh, K.; Kleist, W.; Høj, M.; Jensen, A.D.; Beato, P.; Patzke, G.R.; Grunwaldt, J.D. Systematic study on the influence of the morphology of α-MoO_3 in the selective oxidation of propylene. *J. Solid State Chem.* **2015**, *228*, 42–52. [CrossRef]
119. Volta, J.C.; Tatibouet, J.M. Structure sensitivity of MoO_3 in mild oxidation of propylene. *J. Catal.* **1985**, *93*, 467–470. [CrossRef]
120. Volta, J.C.; Forissier, M.; Theobald, F.; Pham, T.P. Dependence of selectivity on surface structure of MoO_3 catalysts. *Faraday Discuss. Chem. Soc.* **1981**, *72*, 225–233. [CrossRef]
121. Ressler, T.; Walter, A.; Huang, Z.D.; Bensch, W. Structure and properties of a supported MoO_3–SBA-15 catalyst for selective oxidation of propene. *J. Catal.* **2008**, *254*, 170–179. [CrossRef]
122. Khatib, S.J.; Oyama, S.T. Direct oxidation of propylene to propylene oxide with molecular oxygen: A review. *Catal. Rev.* **2015**, *57*, 306–344. [CrossRef]
123. Jin, G.; Lu, G.; Guo, Y.; Guo, Y.; Wang, J.; Liu, X. Epoxidation of propylene by molecular oxygen over modified Ag–MoO_3 catalyst. *Catal. Lett.* **2003**, *87*, 249–252. [CrossRef]
124. Jin, G.; Lu, G.; Guo, Y.; Guo, Y.; Wang, J.; Liu, X. Direct epoxidation of propylene with molecular oxygen over Ag–MoO_3/ZrO_2 catalyst. *Catal. Today.* **2004**, *93–95*, 173–182. [CrossRef]
125. Nguyen, T.K.L.; Ngo, H.H.; Guo, W.; Chang, S.W.; Nguyen, D.D.; Nghiem, L.D.; Liu, Y.; Ni, B.; Hai, F.I. Insight into greenhouse gases emissions from the two popular treatment technologies in municipal wastewater treatment processes. *Sci. Total Env.* **2019**, *671*, 1302–1313. [CrossRef]
126. Han, B.; Yang, Y.; Xu, Y.; Etim, U.J.; Qiao, K.; Xu, B.; Yan, Z. A review of the direct oxidation of methane to methanol. *Chin. J. Catal.* **2016**, *37*, 1206–1215. [CrossRef]
127. Liu, R.S.; Iwamoto, M.; Lunsford, J.H. Partial oxidation of methane by nitrous oxide over molybdenum oxide supported on silica. *J. Chem. Soc. Chem. Commun.* **1982**, *1*, 78–79. [CrossRef]
128. Smith, M.R.; Ozkan, U.S. The partial oxidation of methane to formaldehyde: Role of different crystal planes of MoO_3. *J. Catal.* **1993**, *141*, 124–139. [CrossRef]
129. Arena, F.; Giordano, N.; Parmaliana, A. Working mechanism of oxide catalysts in the partial oxidation of methane to formaldehyde. II. Redox properties and reactivity of SiO_2, MoO_3/SiO_2, V_2O_5/SiO_2, TiO_2, and V_2O_5/TiO_2 systems. *J. Catal.* **1997**, *167*, 66–76. [CrossRef]
130. Taylor, S.H.; Hargreaves, J.S.; Hutchings, G.J.; Joyner, R.W.; Lembacher, C.W. The partial oxidation of methane to methanol: An approach to catalyst design. *Catal. Today* **1998**, *42*, 217–224. [CrossRef]
131. Mohamed, M.; Katib, S.M.A. Structural and catalytic characteristics of MoO_3/CeO_2 catalysts: CO oxidation activity. *Appl. Catal. A* **2005**, *287*, 236–243. [CrossRef]
132. Wang, C.H.; Lin, S.S.; Liou, S.B.; Weng, H.S. The promoter effect and a rate expression of the catalytic incineration of $(CH_3)_2S_2$ over an improved CuO–MoO_3/γ-Al_2O_3 catalyst. *Chemosphere* **2002**, *49*, 389–394. [CrossRef]
133. Huang, X.; Peng, Y.; Liu, X.; Li, K.; Deng, Y.; Li, J. The promotional effect of MoO_3 doped V_2O_5/TiO_2 for chlorobenzene oxidation. *Catal. Commun.* **2015**, *69*, 161–164. [CrossRef]